ACS OMEGA

Open Access

http://pubs.acs.org/journal/acsodf

Article

Design and Characterization of Peptide-Conjugated Solid Lipid Nanoparticles for Targeted MRI and SPECT Imaging of Breast Tumors

Tahereh Rahdari, Hossein Ghafouri,* Sorour Ramezanpour, Mehdi Shafiee Ardestani, and S. Mohsen Asghari*

Cite This: *ACS Omega* 2025, 10, 17310−17326

Read Online

ACCESS | Metrics & More | Article Recommendations | Supporting Information

ABSTRACT: Triple-negative breast cancer (TNBC) presents significant challenges due to its aggressive behavior and lack of targeted treatments. High-resolution imaging techniques and targeted nanoparticles offer potential solutions for early detection and monitoring of TNBC. In this study, we developed and characterized solid lipid nanoparticles (SLNs) conjugated with a C-peptide derived from endostatin to target integrin $\alpha v\beta_3$, overexpressed in TNBC. These SLNs were loaded with superparamagnetic iron oxide nanoparticles (SPIONs) for enhanced magnetic resonance imaging (MRI) and radiolabeled with technetium-99m (^{99m}Tc) for single-photon emission computed tomography (SPECT), enabling dual-modality imaging. Extensive characterization of the nanoparticles was performed utilizing a variety of advanced techniques, including dynamic light scattering (DLS), differential scanning calorimetry (DSC), thermogravimetric analysis (TGA), X-ray diffraction (XRD), vibrating sample magnetometry (VSM), field-emission scanning electron microscopy (FE-SEM), and atomic force microscopy (AFM). This comprehensive analysis validated the successful synthesis and functionalization of the nanoparticles, along with their remarkable magnetic properties, while also revealing their distinct spherical morphology, optimal size, uniform distribution, and colloidal stability. The conjugation of C-peptide significantly enhanced the targeting efficiency in vitro, as evidenced by the MTT and receptor-binding assays in 4T1 cells using flow cytometry and MRI. In vivo studies using a 4T1 murine model demonstrated that peptide-conjugated SLNs accumulated in tumor tissues, providing superior contrast in MRI and enhanced tumor-specific localization in SPECT imaging. Biodistribution analysis confirmed reduced off-target accumulation, particularly in the liver, compared to nontargeted formulations. Collectively, C-peptide-conjugated SLNs provide a promising dual-modality imaging platform for TNBC, offering improved diagnostic accuracy and tumor targeting.

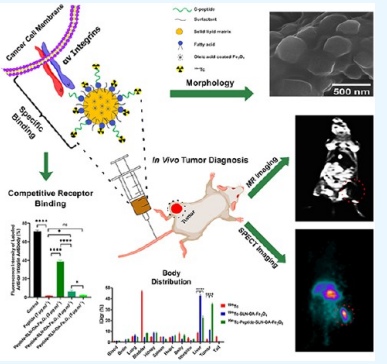

1. INTRODUCTION

The diagnosis and management of breast cancer, particularly triple-negative breast cancer (TNBC), have advanced significantly with the development of enhanced imaging techniques and targeted therapies. TNBC is an aggressive subtype characterized by the absence of estrogen and progesterone receptors and HER2 expression, making it unresponsive to hormonal or HER2-targeted treatments, thus presenting significant clinical challenges.[1,2] Accurate diagnosis and early detection are essential for determining appropriate treatment strategies and improving patient outcomes.[3−6]

Traditional imaging methods such as mammography and magnetic resonance imaging (MRI) are critical for breast cancer detection, but they have limitations, particularly in distinguishing aggressive tumors like TNBC.[7] Recent advancements in molecular imaging techniques, such as single-photon emission computed tomography (SPECT) and MRI, have enabled more detailed insights into tumor biology and facilitated the development of theranostic nanoparticles.[8−11] Solid lipid nanoparticles (SLNs) have emerged as a promising platform for drug delivery and diagnostic imaging due to their high bioavailability, biodegradability, and low toxicity.[12] These nanoparticles can encapsulate imaging agents, enabling them to function as versatile tools for dual-modality imaging.[13,14]

Incorporating superparamagnetic iron oxide nanoparticles (SPIONs) for MRI contrast and radiolabeling SLNs with technetium-99m (^{99m}Tc) for SPECT enables simultaneous high-resolution imaging and real-time biodistribution tracking, addressing the key challenge of accurately targeting tumors in vivo.[15,16] Effective tumor targeting is particularly crucial in TNBC, where rapid progression and metastasis limit the treatment efficacy. Endostatin, an endogenous antiangiogenic

Received: November 7, 2024
Revised: March 17, 2025
Accepted: March 31, 2025
Published: April 22, 2025

protein, has shown significant potential for targeting integrins such as $\alpha v\beta_3$, which are overexpressed in both tumor and endothelial cells, playing a key role in tumor progression and angiogenesis.[15,17−19]

However, the clinical use of full-length endostatin is limited by its instability, insolubility, and high production cost. To address these challenges, we designed a C-peptide that mimics the key functional regions of endostatin while enhancing the stability and maintaining its antitumor properties. The C-terminal segment of endostatin (residues 123−184) was chosen for its ability to suppress cell proliferation, migration, and tumor growth, showing effects similar to the full-length protein.[20] Previous research has identified several critical regions, including residues 1−27, 6−49, 60−70, and 180−199, being essential for endostatin's antiangiogenic and antitumor activities.[20] In designing the C-peptide, we removed nonessential regions that do not significantly contribute to these effects. Specifically, we excluded the β-hairpin region (residues 145−163) and the short β-strand (residues 172−175), along with residues 175−184, which were deemed nonfunctional. The final 30-amino acid sequence, $_2$HN-SDPNGRRLTESYCETWRTEAPSSCHHAYIV-COOH, retains the critical residues necessary for interacting with integrins such as $\alpha v\beta_3$, which are overexpressed in tumor cells and are key targets for antiangiogenic therapy.[17,20] This is the first report of this specific C-peptide in ISI-indexed journals, marking a contribution to the field. Additionally, conjugating this peptide to nanoparticles not only improves its serum stability and half-life but also enhances its targeting effectiveness, making it highly suitable for therapeutic and diagnostic applications.[12]

Nanoparticle conjugation with targeting peptides, such as the C-peptide, is a promising strategy for improving diagnostic accuracy and therapeutic targeting.[21,22] In this study, we developed and evaluated integrin-targeted SLNs conjugated with this C-peptide for use in dual-modality imaging of TNBC. SPIONs were incorporated into the SLNs to improve the MRI contrast, while ^{99m}Tc was used for SPECT imaging, enabling real-time monitoring of biodistribution and tumor targeting.[23] The combination of MRI and SPECT offers complementary imaging modalities, with MRI providing high-resolution anatomical information and SPECT delivering quantitative data on tissue distribution.

The present study aims to evaluate the physicochemical properties, cytotoxicity, and in vivo imaging performance of these peptide-functionalized nanoparticles in TNBC models. By integrating molecular targeting with imaging techniques, we seek to enhance the accuracy and effectiveness of TNBC diagnosis, potentially improving treatment monitoring and patient outcomes.

2. MATERIALS AND METHODS

2.1. Materials. In this study, several high-purity chemicals and reagents were utilized to ensure the integrity and reproducibility of results. Key materials included stearic acid (98% purity, Sigma-Aldrich), and Precirol ATO 5 (Glyceryl distearate, comprising esters of palmitic (C16) and stearic (C18) acids, molecular formula $C_{37}H_{76}O_7$, 99% purity, France, Gattefosse) as the lipid components of of SLN. Additionally, Poloxamer 407 (99% purity, Sigma-Aldrich, Germany), served as a surfactant, and soybean lecithin (≥98% purity, Sigma-Aldrich) was employed as a co-surfactant. For coupling purposes, 1-ethyl-3-[3-(dimethylamino)propyl]carbodiimide hydrochloride (EDC·HCl, 98% purity, Sigma-Aldrich) and *N*-hydroxysuccinimide (NHS, 95% purity, Sigma-Aldrich) were employed. Iron(III) chloride hexahydrate ($FeCl_3{\cdot}6H_2O$, 99% purity, Germany, Merck) and iron(II) chloride tetrahydrate ($FeCl_2{\cdot}4H_2O$, 98% purity, Germany, Merck) were selected as iron oxide precursors. Oleic acid (90% purity, USA, Sigma-Aldrich) served for Fe_3O_4 coating. For cell culture, RPMI-1640 medium, along with fetal bovine serum (FBS, Gibco), trypsin−EDTA, and a penicillin−streptomycin solution were sourced from Gibco. Anti-integrin αv antibodies for targeting studies were of high purity (U.K., Abcam, lot number: GR300208-7). Also, fluorescein (FITC)-conjugated AffiniPure F(ab')2 Fragment Donkey Anti-Rabbit IgG (H+L) was acquired with high purity, suitable for in vitro research, from Jackson ImmunoResearch Laboratories, code number: 711-096-152. Cell lines used in this research included 4T1MCT (4T1 murine mammary carcinoma cell line) and MCF10 (human normal breast epithelial cell line). Both cell lines were supplied by the Pasteur Institute in Tehran. Female athymic BALB/c mice, aged 6−8 weeks and weighing between 20 and 25 g, were ordered from the Institute of Biochemistry and Biophysics at the University of Tehran. Several solvents and additional chemicals were critical to our experimental procedures. Analytical-grade chloroform (99.8% purity), absolute ethanol (99.9% purity), and Tween 20 were employed alongside deionized water, purified using a Milli-Q system (Millipore or equivalent). In peptide synthesis, reagents such as Fmoc-protected amino acids, *N*,*N*-diisopropylethylamine (DIEA), O-(6-chlorobenzotriazol-1-yl)-*N*,*N*,*N*',*N*'-tetramethyluronium hexafluorophosphate (HCTU), *N*,*N*-dimethyl formamide (DMF), dichloromethane (DCM), methanol, piperidine, and 2-chlorotrityl chloride (2-CTC) resin were procured from Sigma-Aldrich. Additionally, potassium bromide (KBr) was employed for FTIR analysis, sodium pertechnetate ($Na^{99m}TcO_4$) and stannous chloride ($SnCl_2$) for radiolabeling, and acetonitrile and trifluoroacetic acid (TFA) for peptide activity. All chemicals and reagents were utilized as received, excluding specific treatment guidelines stated within our methodology.

2.2. Preparation of Nanoparticles. To synthesize Fe_3O_4 magnetic nanoparticles, 0.580 mg of $FeCl_3{\cdot}6H_2O$ and 0.214 mg of $FeCl_2{\cdot}4H_2O$ were dissolved in deionized water and mixed with a vortex mixer. After adding 1.7 mL of ammonia, the mixture was sonicated at 100 W for 30 min and cleaned with an external magnet until achieving a pH of 7.5. This method was modified for enhanced practicality and efficiency.[24] To prepare for loading into SLNs, Fe_3O_4 nanoparticles were first coated with oleic acid. A mixture of 600 μL of oleic acid and a Fe_3O_4 solution was heated at 90 °C for 20 min, promoting oleic acid attachment and causing the nanoparticles to cluster and extract from water. After water removal, the coated nanoparticles were dispersed in absolute ethanol and dried at 65 °C[25] (Figure S1).

Blank SLNs were synthesized using a hot homogenization technique followed by ultrasonication. Initially, the lipid phase was prepared by melting 90 mg of stearic acid and 20 mg of Precirol at 80 °C, to which 10 μL of Tween 20 was added. Concurrently, the aqueous phase was prepared by dispersing 70 mg of soybean lecithin in 3 mL of deionized water, followed by sonication at 70 W for 10 min at 80 °C. Afterward, 80 mg of Poloxamer 407 was incorporated into the lecithin dispersion and stirred for 5 min at 80 °C. The aqueous phase was then gradually added to the lipid phase at 80 °C using a

https://doi.org/10.1021/acsomega.4c10153
ACS Omega 2025, 10, 17310−17326

homogenizer set to 12,000 rpm for 15 min. The resulting mixture was sonicated for an additional 10 min at 70 W, dispersed in 2 mL of distilled water, and sonicated for 15 min at 4 °C. The solution was stored at 4 °C for 24 h to facilitate SLN formation. The final mixture was centrifuged at 14,000 rpm for 20 min, and the resulting pellets were redispersed in fresh deionized water. This procedure was adapted from previous studies with modifications.[26,27]

Synthesis of OA-Fe_3O_4-loaded SLNs (SLN-OA-Fe_3O_4) was done using hot homogenization and ultrasonication. The lipid phase included 90 mg of stearic acid, 20 mg of Precirol, and 10 μL of Tween 20 melted at 80 °C. The aqueous phase was prepared by sonicating 70 mg of soybean lecithin in 3 mL of deionized water at 80 °C, then adding under stirring 80 mg of Poloxamer, followed by dissolving 407.7 mg of OA-Fe_3O_4 in 0.5 mL of chloroform and sonicating at 50 W for 5 min. This solution was combined with the lipid phase, and the aqueous phase was added dropwise at 80 °C while homogenizing at 12,000 rpm for 30 min. The mixture underwent sonication at 70 W for 10 min, then it was dispersed in 2 mL of distilled water and sonicated again for 15 min at 4 °C. After being left at 4 °C for 24 h, it was centrifuged at 14,000 rpm for 20 min, and the pellets were redispersed in fresh deionized water[26,28] (Figure S2).

The C-peptide (2HN-SDPNGRRLTESYCETWR-TEAPSSCHHAYIV-COOH) was synthesized using standard Fmoc solid-phase peptide synthesis on a 2-CTC resin with a loading capacity of 1.0 mmol/g. Sequential coupling of Fmoc-protected amino acids was performed with DIEA and HCTU in anhydrous DMF, followed by washing with DMF, DCM, and methanol. Fmoc groups were removed using a 20% piperidine solution in DMF. The peptide was cleaved from the resin using a TFA cleavage mixture. Purification involved RP-HPLC on a C18 column with a gradient of acetonitrile and water containing 0.1% TFA, achieving over 95% purity, as confirmed by analytical RP-HPLC and molecular-weight verification via electrospray ionization LC−MS. Additional details regarding molecular modeling and LC−MS and HPLC analyses are provided in the Supporting Information, Figures S4−S6.

For the preparation of peptide-conjugated SLNs, the peptide was covalently attached via its N-terminal group to the carboxyl groups of lipids on the surface of SLNs, using EDC and NHS as coupling agents. SLNs (10 mg/mL) were dissolved in a phosphate buffer (pH 7.4) containing EDC (15 mg/mL) and NHS (10 mg/mL) and mixed for 5 min. C-peptide (1 mg/mL) was then added and incubated for 8 h at room temperature while gently shaken at 80 rpm. Excess unbound peptide and EDC−NHS were removed by centrifugation at 14,000 rpm for 15 min (Figure S3).[29]

SLNs were radiolabeled with ^{99m}Tc using a direct labeling technique, employing stannous chloride ($SnCl_2$) as the reducing agent. An acidic $SnCl_2$ solution (300 μg/mL) was prepared and mixed with 0.2 mL of $Na^{99m}TcO_4$ solution (5 mCi radioactivity) at room temperature for 5 min, adjusting the pH to 6−7. Then, 3 mg of peptide-SLN-OA-Fe_3O_4 or SLN-OA-Fe_3O_4 was added, and the mixture was vortexed and stirred for 30 min. Radiochemical purity was evaluated by centrifuging the mixture and measuring the radioactivity in both the supernatant and precipitate. The precipitate was dissolved in fresh buffer saline for use.[30]

2.3. In Vitro Physicochemical Characterization of Nanoparticles. Dynamic light scattering (DLS) measured the HD, polydispersity index (PDI), and ζ-potential of diluted different nanoformulations. The size−time profile of different formulations was measured using DLS. Following the synthesis and drying of Fe_3O_4 and OA-Fe_3O_4 at 65 °C, the nanoparticles were stored at room temperature. Their storage stability was evaluated over a period of 30 days using DLS. Additionally, SLN, SLN-OA-Fe_3O_4, and peptide-SLN-OA-Fe_3O_4 were freeze-dried after synthesis and storage at −20 °C. The stability of these formulations was also assessed through DLS analysis. FTIR spectroscopy analyzed functional groups and interactions in the nanocomplex by blending samples with KBr, compressing them into pellets, and measuring spectra within the range of 4000−400 cm^{-1}. Thermal performance was assessed using differential scanning calorimetry (DSC) and thermogravimetric analysis (TGA). TGA scanned from 0 to 400 °C at 10 °C/min under nitrogen. DSC recorded characteristic peaks and specific heat of melting endotherms for 4 mg samples heated individually. The magnetic aspects of Fe_3O_4, OA-Fe_3O_4, and SLN-OA-Fe_3O_4 were analyzed using a vibrating sample magnetometer at room temperature, with measurements conducted up to a magnetic field strength of 10 kOe.

X-ray diffraction (XRD) was used to analyze the crystal structure and phase of nanoparticles, collecting data from 20−100° (2θ). The particle sizes were estimated using the Scherrer equation based on the XRD data. The formula used is as follows

$$D = \frac{K\lambda}{\beta \cos \theta} \quad (1)$$

where D is the particle size in nanometers, K is the Scherrer constant (0.94), λ is the wavelength of X-ray radiation (1.5406 Å), θ is the corresponding Bragg's diffraction angle, and β is the full width at half-maximum (fwhm) in radians.

Field-emission scanning electron microscopy (FE-SEM) and atomic force microscopy (AFM) analyzed the nanoparticle size and morphology. The amount of OA-Fe_3O_4 incorporated into SLN-OA-Fe_3O_4 was determined using Atomic absorption spectroscopy (AAS). An in vitro magnetic resonance (MR) imaging study was conducted using a Siemens Prisma 3.0 T MR scanner. Various concentrations of SLN-OA-Fe_3O_4 were prepared and mixed with 1% agarose in a 24-well plate, which was placed in water. T2-weighted MR images were obtained with parameters including a repetition time of 5000 ms, echo times ranging from 20 to 320 ms, and a field of view (FOV) of 240 mm × 240 mm. The resulting T2-weighted MR phantom images were quantified using ImageJ software.

2.4. Cell Culture Experiments. In vitro cytotoxicity was evaluated using 4T1MCT and MCF10 normal cell lines in RPMI-1640 medium supplemented with 10% fetal bovine serum and 1% penicillin, maintained at 37 °C in a 5% CO_2 atmosphere. The MTT assay was employed to assess cytotoxicity across various treatments. Once the cells reached 90% confluency, they were detached using 700 μL of trypsin, diluted with medium, and centrifuged at 1400 rpm for 5 min. The supernatant was discarded, and the cell pellets were resuspended in medium with 10% serum. Cells were then seeded at a density of 10,000−15,000 cells per well in a 96-well plate and incubated overnight. The following day, the medium was replaced with fresh media containing different doses of C-peptide, SLN, OA-Fe_3O_4, SLN-OA-Fe_3O_4, peptide-SLN-OA-Fe_3O_4, or culture medium as a negative control for 24 h. MTT powder (5 mg/mL) was added to each well, followed by a 4 h

https://doi.org/10.1021/acsomega.4c10153
ACS Omega 2025, 10, 17310−17326

incubation at 37 °C. After removing the culture medium, formazan crystals were dissolved in DMSO, and absorbance was measured at 595 nm to calculate the IC_{50} value.

Cell viability was also determined using the trypan blue exclusion assay on both 4T1 and MCF10 cells. The cells were seeded in triplicate in cell culture plates at a density of 1×10^5 cells/well and allowed to adhere. After a 24 h adhesion period, the cells were treated with varying concentrations of C-peptide, SLNs, OA-Fe_3O_4, SLN-OA-Fe_3O_4, or peptide-SLN-OA-Fe_3O_4. The cells treated with culture medium alone were considered as the negative control. After a 24 h treatment period, the culture medium was removed, and the cells were washed once with PBS. The cells were then trypsinized, and the cell suspension was mixed with trypan blue solution. The mixture was incubated for 2−3 min at room temperature. The number of viable (unstained) and nonviable (stained blue) cells were counted using a hemocytometer under a light microscope. Viability was calculated using the following formula

$$\text{viability}\ (\%) = \frac{\text{number of viable cells}}{\text{total number of viable and nonviable cells}} \times 100 \quad (2)$$

The binding ability of peptide-bound nanoparticles to αv integrin receptors was investigated using flow cytometry. Initially, 4T1 cultured cells were collected, centrifuged, and then resuspended in fresh medium supplemented with 10% FBS. Each well of a 12-well plate was seeded with 300,000 cells and treated with control (no treatment), peptide (70% of the IC_{50} dose, 7 $\mu g \cdot mL^{-1}$), peptide-SLN-OA-Fe_3O_4 (at 30, 50 and 70% doses of IC_{50}, corresponding to 2, 4, and 6 $\mu g \cdot mL^{-1}$, respectively), and a constant dose of anti-integrin αv antibody (400 $ng \cdot mL^{-1}$). After 3 h of incubation, an equal amount of FITC-labeled secondary antibody (400 $ng \cdot mL^{-1}$) was added to the mixture and allowed to interact with the cells for 1 h. The cellular contents of each well were then centrifuged to remove unbound probes and resuspended in fresh medium. The interactions were analyzed using flow cytometry.[21,22,31,32] The binding ability of peptide-bound nanoparticles to αv integrin receptors was investigated using MR imaging. 4T1 cultured cells were harvested, centrifuged, and resuspended in fresh medium with 10% FBS. Each well of a 24-well plate was filled with 200,000 cells and subject to various treatments: the control medium, SLN-OA-Fe_3O_4, and peptide-SLN-OA-Fe_3O_4. The treatments were administered at a concentration of 70% of IC_{50}, specifically at 6 μg/mL. In additional assays, cells were treated with peptide-SLN-OA-Fe_3O_4 and three doses of anti-integrin αv antibody (100, 200, and 400 $ng \cdot mL^{-1}$). After 4 h of incubation for nanoparticle−cell interaction, the wells were centrifuged to remove unbound probes and resuspended in fresh medium. T2-weighted MR images were then acquired using a 3.0 T MR scanner to assess the interactions.[33] To achieve maximum cell viability and optimal receptor binding, 70% concentration of the IC_{50} for peptide-SLN-OA-Fe_3O_4 was utilized. The concentration of the control antibodies was determined to be 400 ng/mL, based on the preliminary testing. These experiments demonstrated that this specific concentration was optimal for maximizing binding to the αv integrin receptors, thereby ensuring the accuracy and reliability of our experimental measurements.

2.5. In Vivo Experiments. Tumor targeting was evaluated through in vivo MR Imaging. All procedures involving the animals adhered to the ethical standards set by the University of Tehran's Ethics Committee for Animal Research, and approval was granted by the Biomedical Research Ethics Committee of the University of Guilan, under code number: IR.GUILAN.REC.1401.010. In vivo T2-weighted MR imaging was performed using a 3.0 T MR scanner on mice with 4T1 tumors implanted in their left legs, reaching a size of 300 mm^3. Mice were randomly assigned to two treatment groups: SLN-OA-Fe_3O_4 (n = 3) and peptide-SLN-OA-Fe_3O_4 (n = 3). Anesthesia was induced with ketamine and xylazine. Initially, untreated mice underwent T2-weighted MR imaging as controls. Following that, each treatment group received 100 μL of their respective nanoparticle solution (each solution containing 1 $mg \cdot mL^{-1}$ Fe_3O_4) via tail vein injection, with imaging conducted at 30, 60, and 180 min post-treatment.

To further assess tumor targeting, we conducted in vivo SPECT Imaging. Nanoparticles labeled with ^{99m}Tc were intravenously injected into 4T1 breast tumor-bearing BALB/c mice for SPECT imaging (n = 3). The administered activity was standardized to approximately 1.2 mCi (1.2 mL dose). One hour postinjection, three-dimensional (3D) spectral imaging was conducted to evaluate the in vivo biodistribution of free ^{99m}Tc, comparing it with ^{99m}Tc-SLN-OA-Fe_3O_4 and ^{99m}Tc-peptide-SLN-OA-Fe_3O_4 nanoparticles.

2.6. Ex Vivo Studies. After MR imaging, a biodistribution study was conducted to assess the accumulation of Fe_3O_4-based nanoparticles in various tissues using Prussian blue staining. Microscopy images were obtained with an inverted fluorescence microscope. Following SPECT imaging, tissue samples were harvested to measure their radioactivity uptake using a dose calibrator. To calculate the blood clearance of the ^{99m}Tc -labeled SLNs, the following formula was utilized

$$\text{clearance} = \frac{\text{dose}}{L \times C} \quad (3)$$

where the term dose is defined as the amount of technetium administered, L represents the dosing interval, and C indicates the concentration of technetium in the plasma.

Additionally, an exponential decay model was used to describe the activity of technetium over time

$$A = A_0 e^{-\lambda t} \quad (4)$$

where A is the end activity, A_0 is the initial activity, e is a mathematical constant approximately equal to 2.71828, and λ is the decay constant, which indicates the rate of decay and is calculated using the formula $\lambda = 0.693/T_{1/2}$, where $T_{1/2}$ is the half-life of ^{99m}Tc (6 h) and t is the time elapsed since administration.

Following the injection of SLN-Fe_3O_4 and peptide-SLN-OA-Fe_3O_4 nanoparticles, 4T1MCT-bearing mice underwent biosafety evaluation at 3 h postinjection. The mice, including healthy controls, were ethically euthanized. Tissue samples were harvested, fixed in 10% paraformaldehyde, and subjected to H&E staining for histological examination.

2.7. Statistical Analysis. Data analysis, graph generation, and statistical evaluation were conducted using Prism software (version 8.0.2), and results are presented as mean ± SEM. One-way ANOVA with Tukey's post hoc test assessed significant differences for one independent variable, while two-way ANOVA was employed for testing two independent variables. Statistical significance was established at a 95% confidence level ($P < 0.05$). Image quantification utilized ImageJ 1.52v software.

https://doi.org/10.1021/acsomega.4c10153
ACS Omega 2025, 10, 17310−17326

a

	Fe_3O_4	OA-Fe_3O_4	SLN	SLN–OA-Fe_3O_4	Peptide-SLN-OA-Fe_3O_4
Zeta potential (mV)	-7±1	-22±0.5	-22	-23±2	-12±2
Mean size (nm)	67	200	243	315	347
PDI	0.3	0.3	0.3	0.3	0.3

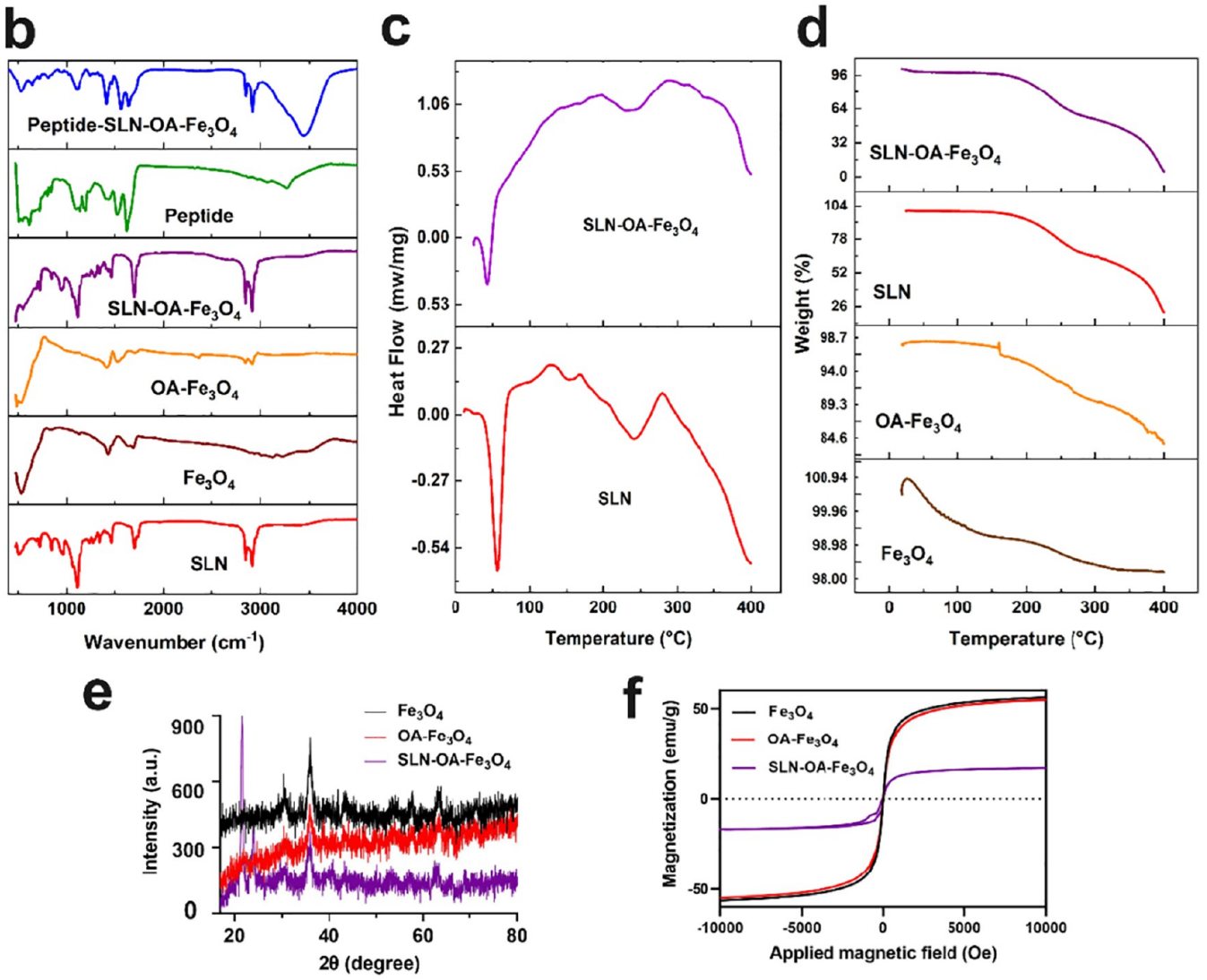

Figure 1. Characterization of nanoparticles. (a) ζ-Potential, mean size, and PDI of nanoparticles assessed using DLS; see Figures S2 and S3 for details. (b) FTIR spectra (500−4000 cm^{-1}) revealing functional groups in nanoparticles. (c) DSC analysis, demonstrating the thermal properties of SLN and SLN-OA-Fe_3O_4. (d) TGA curves illustrating the thermal stability of the nanoparticles. (e) XRD analysis indicating the crystal structure and phase purity of the nanoparticles. (f) Magnetic properties of the nanoparticles assessed by vibrating sample magnetometry (VSM).

3. RESULTS AND DISCUSSION

3.1. Characterization of Nanoparticles. The size, morphology, and surface electrostatic properties of nanoparticles significantly influence their bodily clearance, tissue distribution, and cellular uptake. Spherical nanoparticles below 500 nm enhance the internalization efficiency by effectively attaching to cells and delivering a high drug payload.[34] The SLN size, surface charge, and uniformity were assessed using DLS. The DLS results revealed the following mean sizes and polydispersity indexes (PDIs) for various nanoparticles: Fe_3O_4 (67 nm, PDI: 0.3), OA-Fe_3O_4 (200 nm, PDI: 0.3), blank-SLN (243 nm, PDI: 0.3), OA-Fe_3O_4−SLN (315 nm, PDI: 0.3), and peptide-conjugated SLN-OA-Fe_3O_4 (347 nm, PDI: 0.3). PDI values lower than 0.3 indicate a homogeneous particle size distribution.[35] ζ-Potential assesses nanoparticles' surface

https://doi.org/10.1021/acsomega.4c10153
ACS Omega 2025, 10, 17310−17326

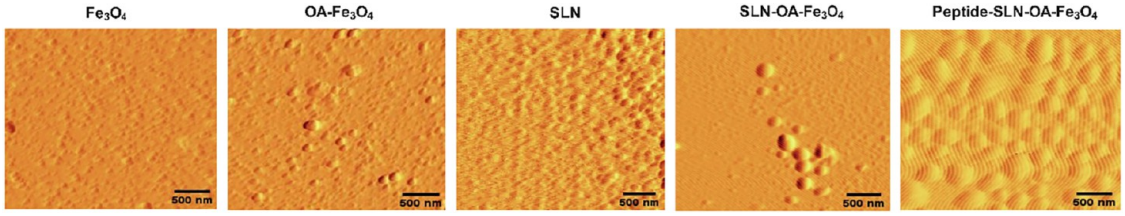

Figure 2. Morphological characterization of Nanoparticles. AFM images show spherical and homogeneous nanoparticles. Scale bar: 500 nm (n = 3).

electrical properties and charge interactions with the medium. In this study, the ζ-potential of Fe_3O_4 was measured at −7 mV, which increased to −22 mV upon oleic acid coating, indicating successful decoration with carboxylate groups. The ζ-potential for blank-SLN was −22 mV, while that of SLN-OA-Fe_3O_4 was −23 mV, showing no significant differences and confirming that OA-Fe_3O_4 was well encapsulated in SLN without affecting colloidal stability. When the peptide was conjugated to SLN-OA-Fe_3O_4, the surface charge decreased to −12 ± 2 mV, indicating amide coupling between the carboxylate groups on SLN and the peptide's amino terminus, which shielded some carboxyl groups. The negative surface charge of nanoparticles induces electrostatic repulsion, leading to physical stability during storage and preventing aggregation[36] (see Figures 1a, S8, and S9 in the Supporting Information for additional data). Previous studies show that negatively charged nanoparticles improve anticancer drug delivery efficiency by reducing clearance and enhancing blood compatibility through electrostatic repulsion.[37] The uniform size distribution, stable surface charge, and successful incorporation of OA-Fe_3O_4 and peptide suggest that these nanoparticles are well suited for biomedical applications. After a 1 month storage period of different nanoformulations, the mean size of the nanoparticles was evaluated using DLS. The measurements revealed that the size of the nanoparticles remained largely unchanged from the initial values. These results indicate that the nanoparticles maintained their stability throughout the storage period (Figure S10). In addition, after a 4 month storage period at −20 °C, the mean size, PDI, and ζ-potential of peptide-SLN-OA-Fe_3O_4 was evaluated with DLS. The measurements revealed that the size and ζ-potential of the nanoparticles remained largely unchanged from the initial values. These results indicate that peptide-SLN-OA-Fe_3O_4 maintained their stability throughout the storage period (data not shown).

The possible interactions among the components, bonding patterns, and surface functionalization of the nanoparticles were studied using FTIR spectroscopy (Figure 1b). The FTIR spectra span from 475 to 4000 cm^{-1}. In blank-SLN, key peaks include 2920 and 2854 cm^{-1} (C−H stretching in $-CH_2$ groups), 1710 cm^{-1} (C═O stretching), 1110 cm^{-1} (C−O−C stretching), and 3400 cm^{-1} (O−H stretching).[38,39] Fe_3O_4 shows a characteristic band at 544 cm^{-1} (Fe−O vibration).[40] Fe_3O_4 coated with oleic acid (OA) is indicated by peaks at 2930 and 2850 cm^{-1} (CH_3 stretching), and a shift of the C═O peak from 1702 to 1650 cm^{-1} indicates the interaction with Fe atoms.[25] For peptide−SLN conjugates, characteristic peaks are observed at 1645 cm^{-1} (amide C═O stretching) and 1511 cm^{-1} (N−H bending), confirming peptide conjugation.[17]

DSC measured the heat flow associated with thermal transitions. The endothermic melting peaks of stearic acid and precirol at 53 °C indicate that the lipid core in blank-SLN and SLN-OA-Fe_3O_4 is in a solid state (Figure 1c).

Figure 1d presents the TGA profiles for four different samples: Fe_3O_4, OA-Fe_3O_4, SLN, and SLN-OA-Fe_3O_4. The iron oxide nanoparticles (Fe_3O_4) display remarkable thermal stability with minimal weight loss (approximately 2%) up to 400 °C, likely due to the removal of adsorbed moisture.[41] The oleic acid-coated iron oxide (OA-Fe_3O_4) demonstrates a moderate weight loss beginning around 200 °C, amounting to approximately 15%, which can be attributed to the thermal decomposition of the oleic acid layer.[25,42] In contrast, SLN exhibits a significant weight loss of approximately 70−80% within the temperature range of 200−400 °C, correlating with the thermal breakdown of lipid constituents, including Precirol, lecithin, stearic acid, and Poloxamer 407. The SLN-OA-Fe_3O_4 sample shows a similar reduction in mass (75−80% weight loss) within the same temperature range, confirming the successful encapsulation and integration of oleic acid-coated Fe_3O_4 within the SLN matrix.

The crystal structure and phase purity of the nanoparticles were analyzed by XRD (Figure 1e). The Fe_3O_4 nanoparticles exhibit distinct peaks at 30.1° (220), 35.5° (311), 43.1° (400), 53.4° (422), 57° (511), and 62.2° (440), aligning with the Fe_3O_4 phase, as documented in the existing research.[11,43] In the OA-Fe_3O_4 pattern, these characteristic peaks were reduced, confirming the presence of OA over Fe_3O_4.[10,44] After encapsulating Fe_3O_4 in SLNs, the diffraction peaks became noisier and diminished, indicating successful encapsulation.[45] The sizes of the nanoparticles were evaluated using the Scherrer equation based on the XRD data. For Fe_3O_4, the most intense diffraction peak is located at 35.5° with a fwhm (β) of 0.002178 radians, resulting in a calculated particle size of approximately 70 nm. For OA-Fe_3O_4, the most intense diffraction peak is also observed at 35.5° with a fwhm of 0.000763 radians, yielding a calculated particle size of approximately 200 nm. For SLN-OA-Fe_3O_4, the most intense diffraction peak is located at 25° with a fwhm of 0.000444 radians, leading to an estimated particle size of approximately 320 nm. These calculated sizes are consistent with the results obtained from DLS analysis, further validating our findings.

Having magnetic properties is a crucial parameter for an MRI contrast agent.[33,46] Therefore, the magnetic characteristics of the synthesized nanoparticles were evaluated using a VSM (Figure 1f). The saturation magnetization values were approximately 56 emu/g for Fe_3O_4, around 55 emu/g for OA-Fe_3O_4, and approximately 16 emu/g for SLNs containing OA-Fe_3O_4, suggesting successful encapsulation of OA-Fe_3O_4. The magnetic properties of Fe_3O_4, OA-Fe_3O_4, and SLN-OA-Fe_3O_4 in response to an external magnet are illustrated in Figure S7a−d.

The morphology of the nanoparticles was investigated using both AFM and FE-SEM techniques. Micrographs revealed spherical and uniform-sized nanoparticles, suitable for drug delivery. Morphological analysis showed that the conjugation

https://doi.org/10.1021/acsomega.4c10153
ACS Omega 2025, 10, 17310−17326

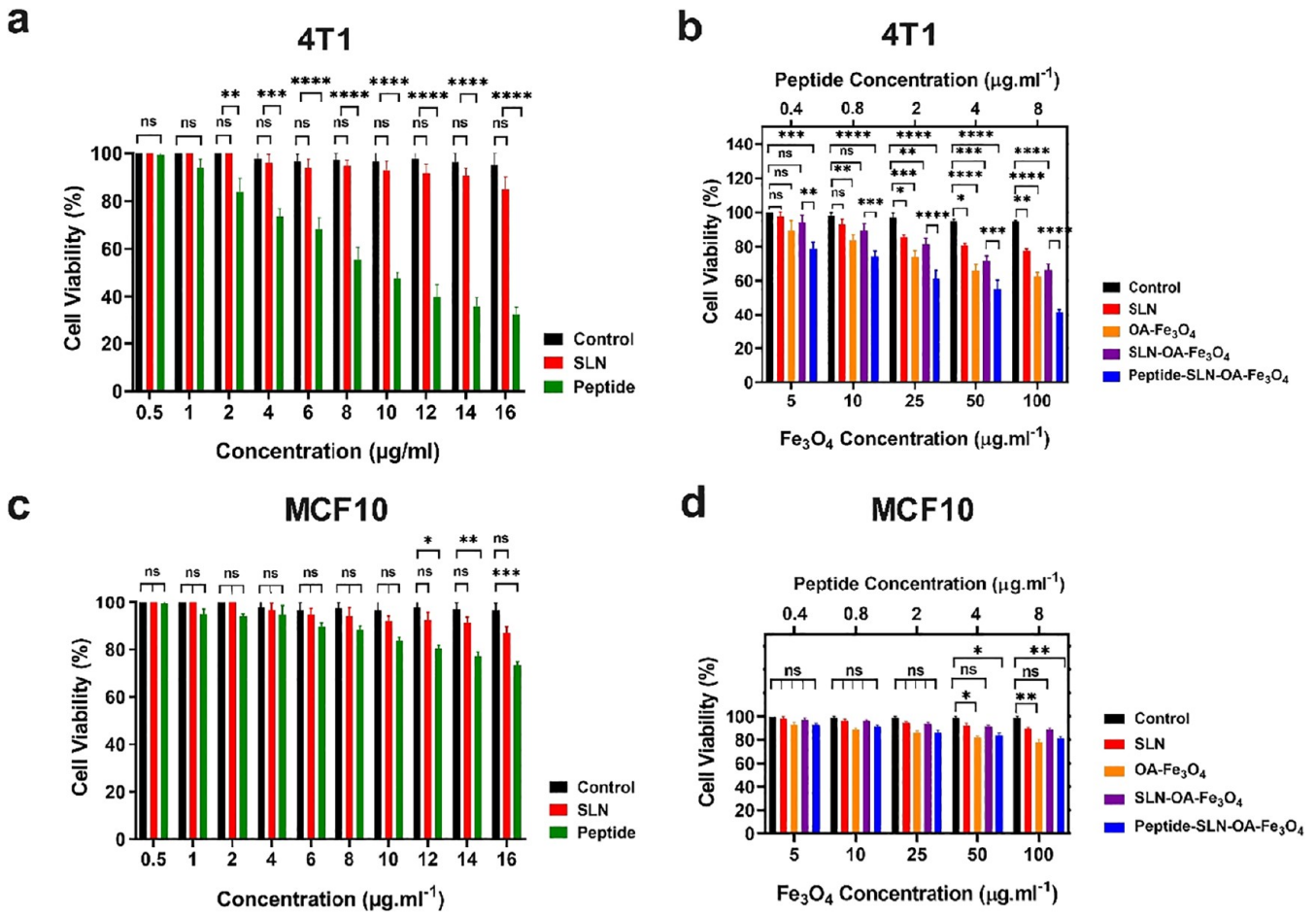

Figure 3. Cell viability. (a) Viability of 4T1MCT cells treated with different concentrations of free peptide (0.5, 1, 2, 4, 6, 8, 10, 12, 14, and 16 $\mu g \cdot mL^{-1}$) after 24 h. (b) Viability of 4T1MCT cells treated with SLN, OA-Fe_3O_4, SLN-OA-Fe_3O_4, and peptide-SLN-OA-Fe_3O_4 at different concentrations over 24 h. (c) Viability of MCF10 normal cells treated with different concentrations of free peptide (0.5, 1, 2, 4, 6, 8, 10, 12, 14, and 16 $\mu g \cdot mL^{-1}$) after 24 h. (d) Viability of MCF10 normal cells treated with SLN, OA-Fe_3O_4, SLN-OA-Fe_3O_4, and peptide-SLN-OA-Fe_3O_4 at different concentrations over 24 h. Cell viability was measured through the MTT assay, and data were analyzed with Prism 8 software (two-way ANOVA, mean ± SEM, $n = 3$, $^{****}P < 0.0001$, $^{***}P < 0.001$, $^{**}P < 0.01$, $^{*}P < 0.05$, or ns: not significant).

of peptide and entrapment OA-Fe_3O_4 did not alter the SLN shape. The nanoparticle sizes matched with DLS measurements (Figures 2 and S11).

3.2. In Vitro Cytotoxicity. The development of safe and effective imaging tracers is crucial for advancing noninvasive diagnostic techniques. The MTT assay was conducted on 4T1MCT cells to evaluate the cytotoxic effects of various nanoparticle formulations after 24 h of treatment. The free C-peptide demonstrated an IC_{50} value of 10.7 $\mu g \cdot mL^{-1}$, which can be attributed to its intrinsic targeting properties and antitumor effects (Figure 3a). In contrast, the blank-SLN, OA-Fe_3O_4, and SLN-OA-Fe_3O_4 formulations demonstrated significant biocompatibility, as they did not exhibit substantial cytotoxicity at the highest concentrations tested (Figure 4b). The treatments containing OA-Fe_3O_4 resulted in lower cell viability compared to the treatments with SLNs alone. However, when OA-Fe_3O_4 was incorporated into SLNs, there was a notable improvement in cell viability. This enhancement suggests that the inclusion of OA-Fe_3O_4 within the SLN matrix is beneficial for mitigating the inherent toxicity of OA-Fe_3O_4, potentially due to a controlled release mechanism or improved cellular interactions. Interestingly, when examining the peptide-SLN-OA-Fe_3O_4 formulation, which incorporates 100 $\mu g/mL$ OA-Fe_3O_4 and 8 $\mu g/mL$ conjugated C-peptide, a more pronounced impact on 4T1 cell viability was observed, showing a 55% reduction (Figure 3b). This suggests that while SLNs enhance the overall biocompatibility and decrease the cytotoxicity of OA-Fe_3O_4, the addition of the C-peptide alters the formulation's interaction against the integrin receptors on TNBC cells.

The MTT assay was also performed on MCF10 (human normal breast epithelial cells) to assess the biocompatibility of C-peptide and nanoparticles. All treatments exhibited considerably lower cytotoxicity toward MCF10 normal cells compared to tumor cells. Specifically, cell viability was maintained at 89 and 80% for C-peptide and peptide-SLN-OA-Fe_3O_4 formulations, respectively (Figure 3c,d).

Additionally, cell viability was assessed using the trypan blue exclusion assay. As illustrated in Figure S12, the viability of 4T1 cancer cells was reduced to 34% when treated with the highest concentration of peptide-SLN-OA-Fe_3O_4 nanoparticles. In contrast, MCF10 cells retained a viability of 86% under the same conditions. These findings are consistent with the results obtained from the MTT assay, reinforcing the selectivity of the peptide-SLN-OA-Fe_3O_4 formulation. Therefore, the peptide-SLN-OA-Fe_3O_4 nanoparticles demonstrate an ability to effectively distinguish between healthy and cancerous tissues. This selectivity suggests a reduced risk of adverse side

https://doi.org/10.1021/acsomega.4c10153
ACS Omega 2025, 10, 17310−17326

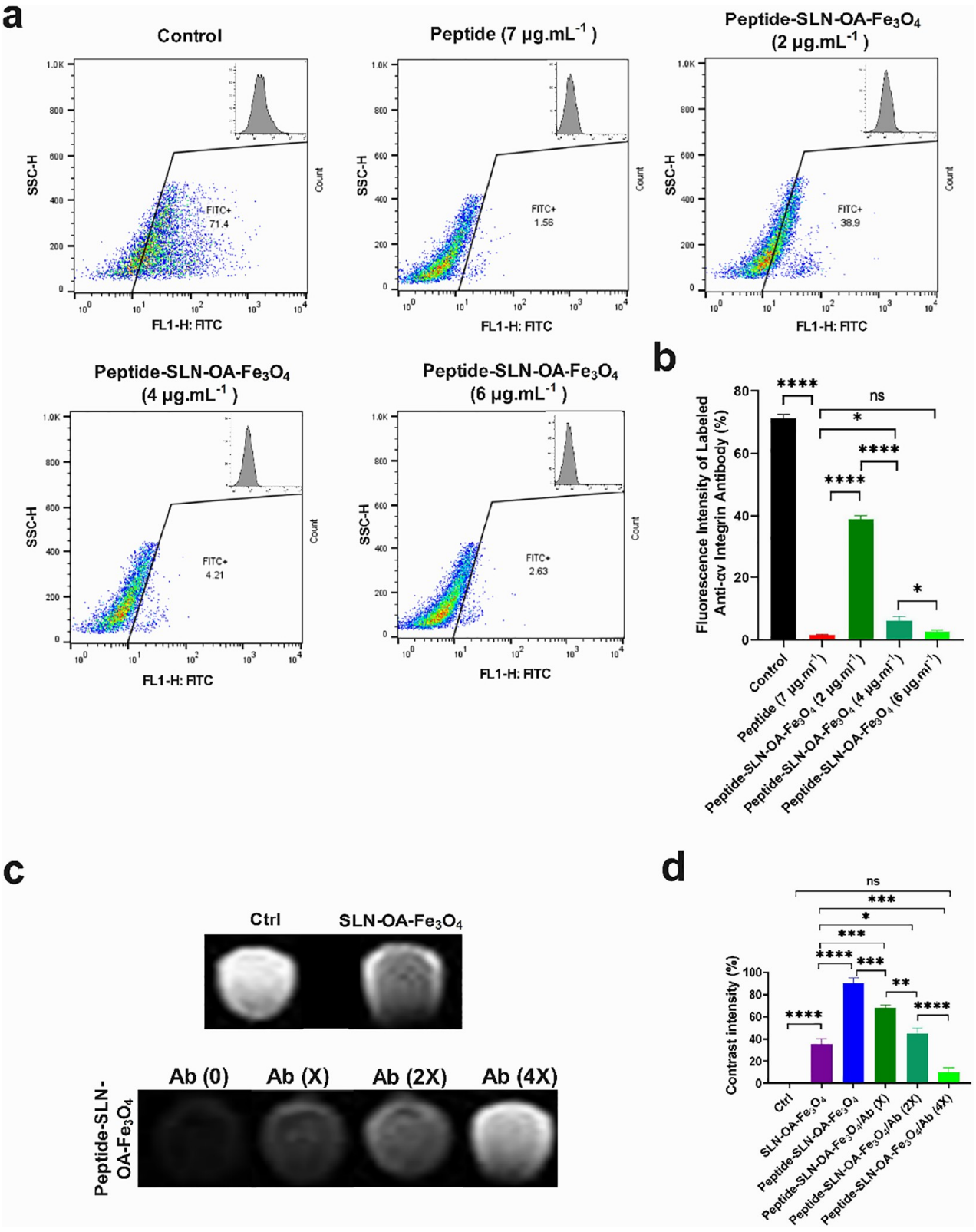

Figure 4. Binding specificity studies. (a) Receptor-binding assays using flow cytometry. 4T1MCT cells were incubated with free peptide (7 $\mu g \cdot mL^{-1}$) and peptide conjugated on SLN (peptide-SLN-OA-Fe_3O_4) at different concentrations (0, 2, 4, and 6 $\mu g \cdot mL^{-1}$). After adding the anti-integrin αv antibody and FITC-conjugated secondary antibody, flow cytometric analysis was performed. (b) Quantitative analysis of the flow cytometry assay using Prism 8 software (two-way ANOVA, mean ± SEM, $n = 3$, ****$P < 0.0001$, ***$P < 0.001$, **$P < 0.01$, *$P < 0.05$, or ns: not significant). (c) Evaluation of the targeting capability of peptide-SLN-OA-Fe_3O_4 using MRI. Harvested 4T1 cells were incubated with peptide-SLN-OA-Fe_3O_4 and varying doses of anti-integrin αv antibody ($X = 100$ ng/mL). MR images show a decreased T_2 signal in 4T1 cell phantoms by increasing doses of the anti-integrin αv antibody. (d) Quantitative analysis was performed using ImageJ and Prism 8 software (two-way ANOVA, mean ± SEM, $n = 3$, ****$P < 0.0001$, ***$P < 0.001$, **$P < 0.01$, *$P < 0.05$, or ns: not significant).

https://doi.org/10.1021/acsomega.4c10153
ACS Omega 2025, 10, 17310−17326

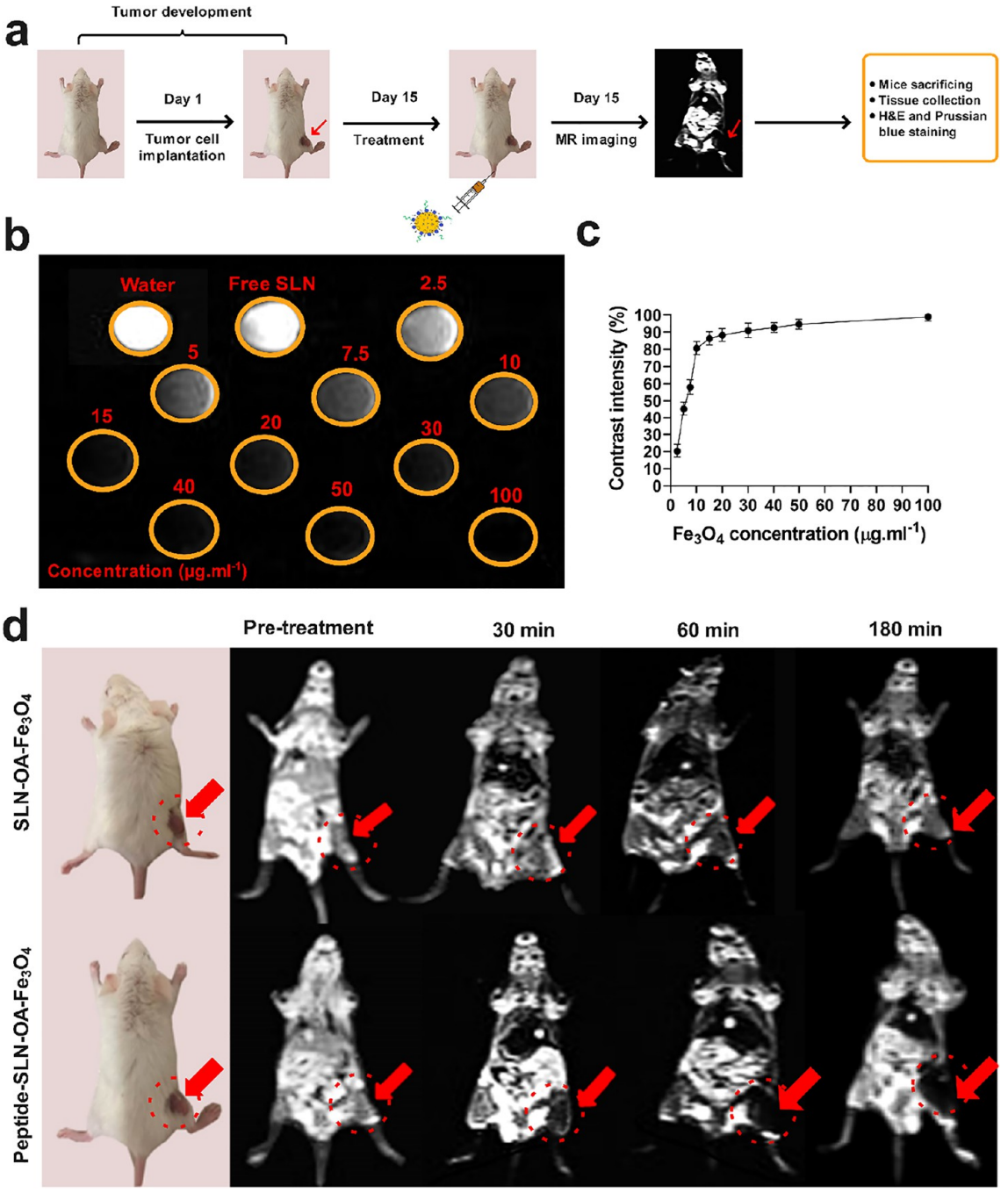

Figure 5. Binding and targeting efficacy through MR imaging. (a) Schematic figure of in vivo MR imaging protocols. (b) T2-weighted MR images of increasing Fe_3O_4 concentration loading into SLN ($\mu g \cdot mL^{-1}$) ($n = 3$). (c) Contrast intensity of T2-weighted MR images quantified using ImageJ software ($n = 3$). (d) In vivo MRI of 4T1MCT-bearing Balb-c mice. MR images were taken at various intervals following the tail vein injection of SLN-OA-Fe_3O_4 and peptide-SLN-OA-Fe_3O_4 ($n = 3$).

effects and enhances the potential safety of these nanoparticles for targeted diagnostic applications.

Consistent with previous studies, breast tumor-targeting peptides exhibit significant cytotoxic effects on 4T1 cancer cells due to their selective binding to overexpressed receptors while having a minimal impact on normal breast MCF10 cells. This differential effect is crucial for achieving targeted therapeutic outcomes without compromising the viability of healthy tissues.[15,47]

3.3. Binding Specificity. To investigate the binding specificity of peptide-SLN-OA-Fe_3O_4, its binding position was investigated using flow cytometry. For this purpose, control and peptide (at a concentration of 70% IC_{50}, 7 $\mu g \cdot mL^{-1}$), as well as peptide-SLN-OA-Fe_3O_4 in a gradient concentration (30, 50, and 70% of IC_{50}, corresponding to 2, 4, and 6 $\mu g \cdot mL^{-1}$, respectively), were treated with 4T1 cells. The primary anti-integrin αv antibody (400 $ng \cdot mL^{-1}$) was also added to the mixtures. Subsequently, after 3 h, a FITC-labeled secondary antibody (400 $ng \cdot mL^{-1}$) was introduced, allowing 1 h for binding to the primary antibodies. Washing was performed to remove any unbound probe. The fluorescence intensity of the secondary antibody was then analyzed using

https://doi.org/10.1021/acsomega.4c10153
ACS Omega 2025, 10, 17310−17326

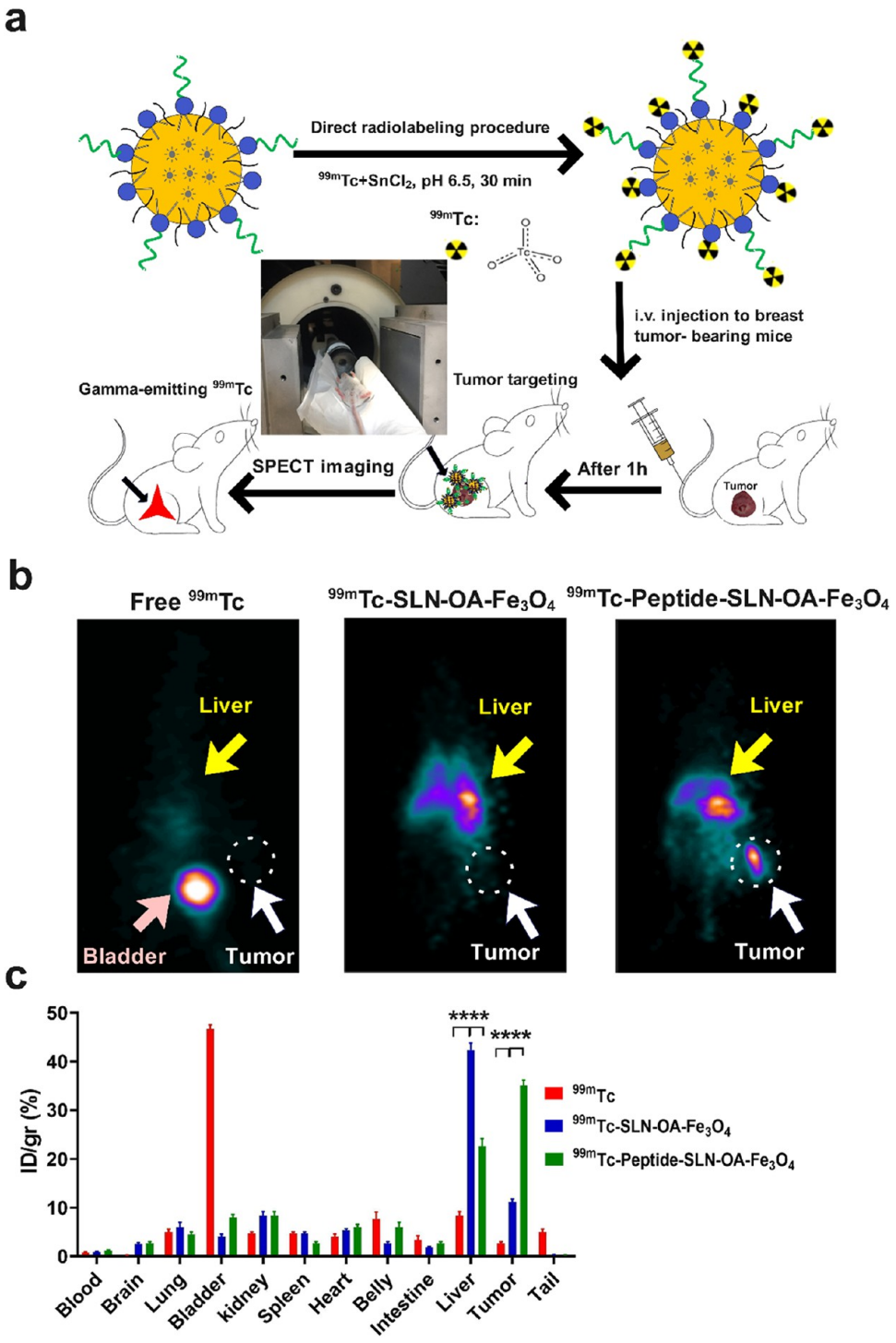

Figure 6. In vivo SPECT imaging. (a) Schematic of radiolabeling and in vivo SPECT imaging protocols. (b) 3D SPECT imaging of 4T1MCT-bearing Balb/c mice showing that ^{99m}Tc-peptide-SLN-OA-Fe_3O_4 accumulated effectively in tumors compared to ^{99m}Tc-SLN-OA-Fe_3O_4. Free ^{99m}Tc exhibited a short half-life, rapidly excreting into the bladder. (c) Tissue distribution of free ^{99m}Tc, ^{99m}Tc-SLN-OA-Fe_3O_4, and ^{99m}Tc-peptide-SLN-OA-Fe_3O_4 in treated mice measured by a dose calibrator after their sacrifice. The data were analyzed by two-way ANOVA using Prism software (mean ± SEM, $n = 3$, ****$P < 0.0001$, ***$P < 0.001$, **$P < 0.01$, *$P < 0.05$, or ns: not significant).

flow cytometry. As observed, in the absence of peptide (control), the highest binding of the primary antibody to the αv integrin receptors was noted, resulting in the greatest fluorescence intensity from the secondary antibody. An increase in the concentration of peptide-SLN-OA-Fe_3O_4 resulted in a decrease in the fluorescence intensity of the secondary antibody, confirming the specificity of the peptide for the αv integrin receptors. A concentration of 70% IC_{50} (in free peptide and peptide-SLN-OA-Fe_3O_4) likely occupied most available binding sites for the primary antibody, leading to an absence of detectable fluorescence intensity (Figure 4a,b). To gain a deeper understanding of the binding sites of the drug delivery system, we conducted in vitro magnetic resonance (MR) imaging studies on 4T1 cells that overexpress integrin

https://doi.org/10.1021/acsomega.4c10153
ACS Omega 2025, 10, 17310−17326

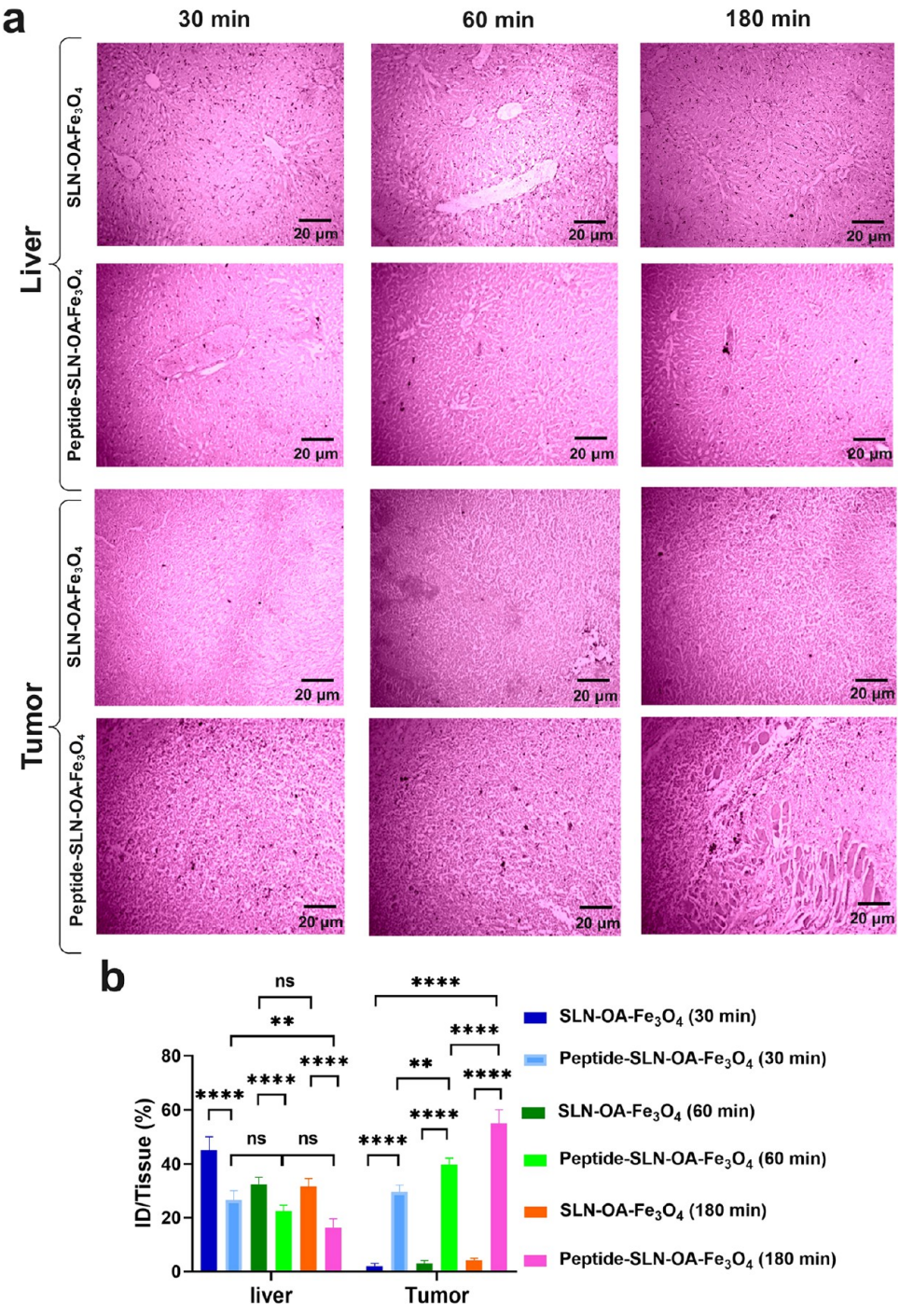

Figure 7. Biodistribution study. (a) Prussian blue staining was performed on tumor and liver tissues from 4T1MCT-bearing BALB/c mice at 30, 60, and 180 min postinjection of SLN-OA-Fe_3O_4 and peptide-SLN-OA-Fe_3O_4; scale bar: 20 μm. Significant iron particle accumulation was observed in the tumors of peptide-SLN-OA-Fe_3O_4-treated mice, increasing over time, while SLN-OA-Fe_3O_4-treated mice showed minimal uptake. Additionally, the peptide formulation resulted in lower liver accumulation compared to SLN-OA-Fe_3O_4. (b) Microscopy analysis using ImageJ quantified the iron particles, and data were analyzed with two-way ANOVA using Prism software (mean ± SEM, $n = 3$, ****$P < 0.0001$, ***$P < 0.001$, **$P < 0.01$, *$P < 0.05$, or ns: not significant).

$\alpha v\beta_3$. MR imaging showed that peptide-SLN-OA-Fe_3O_4-treated cells exhibited significantly enhanced signal contrast compared to cells treated with nontargeted SLN-OA-Fe_3O_4, confirming specific binding to the $\alpha v\beta_3$ integrin receptors (Figure 4c,d). Additionally, a higher concentration of anti-integrin αv antibody reduced the binding of peptide-SLN-OA-Fe_3O_4, as evidenced by a marked decrease in MR signal intensity. This confirms the specificity of the peptide for αv integrins and highlights its potential for precise targeting in TNBC diagnostic applications. These results align with earlier research, which also used competitive binding assays to verify nanoparticle targeting.[21,22,31−33,46]

3.4. In Vivo MRI. Figure 3a illustrates the in vivo MR imaging protocols. T2-weighted images revealed that SLNs containing OA-Fe_3O_4 exhibit excellent superparamagnetic properties, leading to concentration-dependent negative

https://doi.org/10.1021/acsomega.4c10153
ACS Omega 2025, 10, 17310−17326

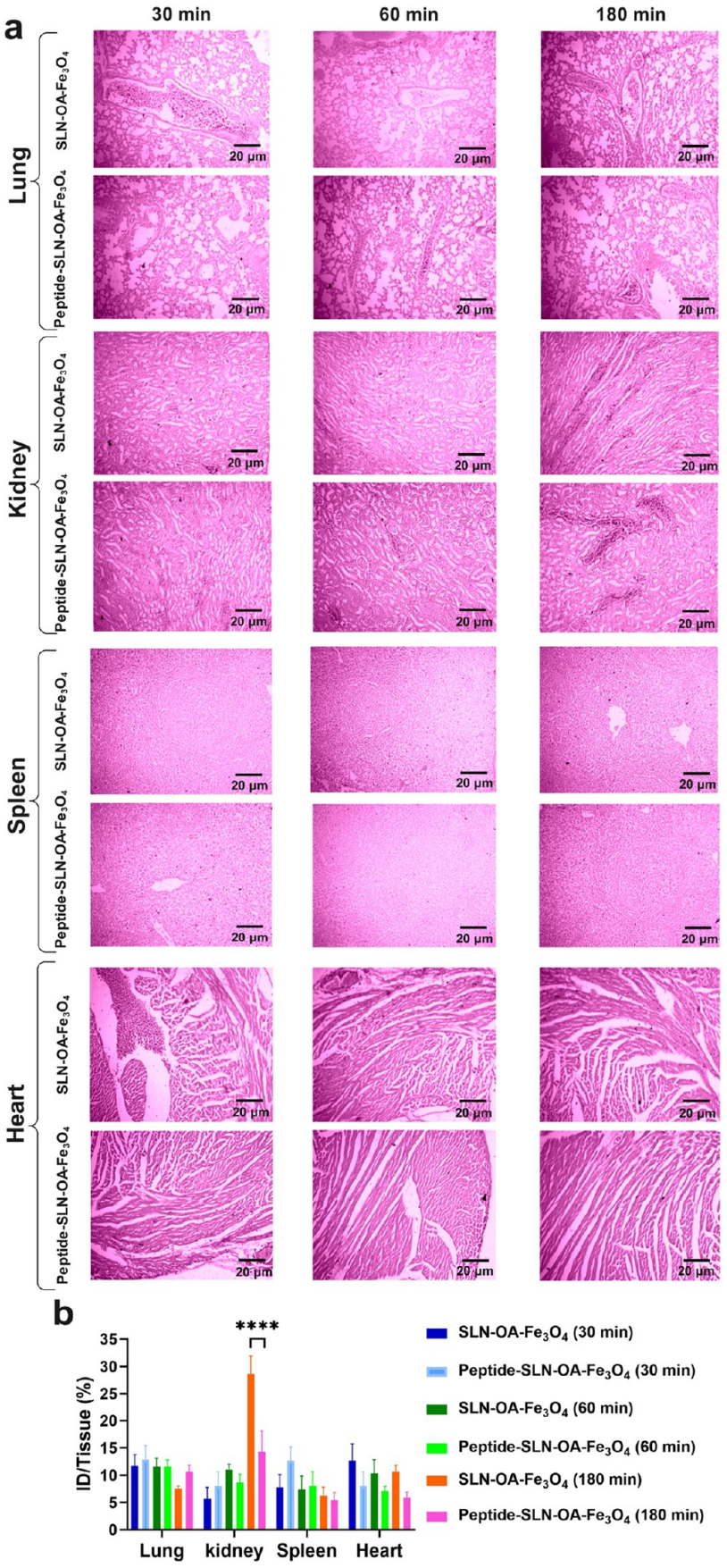

Figure 8. (a) Microscopic view of Prussian blue staining, scale bar: 20 μm. (b) Quantitative analysis of iron accumulation in the lung, kidney, spleen, and heart of treated mice. Data were analyzed using two-way ANOVA using Prism software (mean ± SEM, $n = 3$, ****$P < 0.0001$, ***$P < 0.001$, **$P < 0.01$, *$P < 0.05$, or ns: not significant).

https://doi.org/10.1021/acsomega.4c10153
ACS Omega 2025, 10, 17310−17326

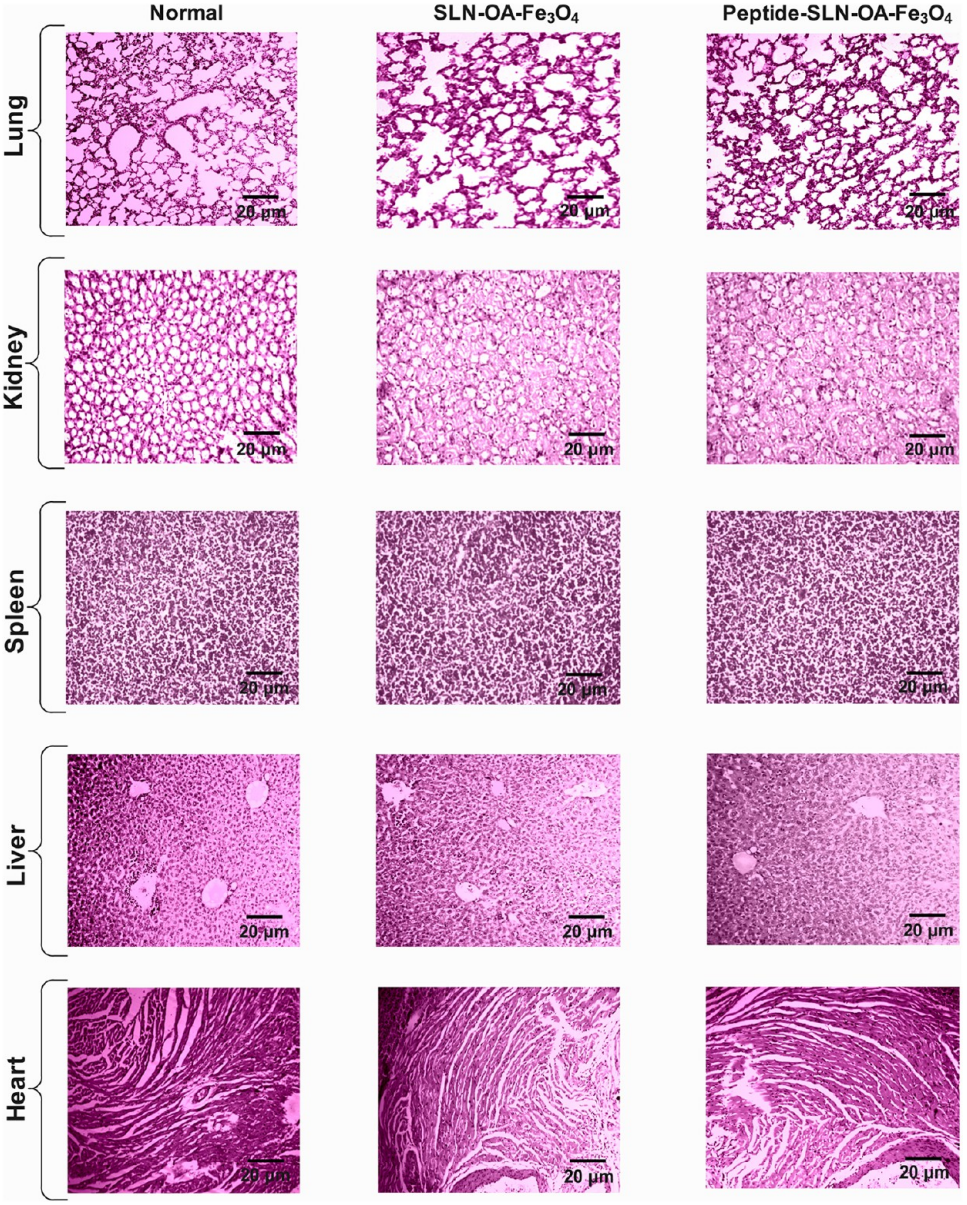

Figure 9. H&E staining of tissues from SLN-OA-Fe_3O_4- and peptide-SLN-OA-Fe_3O_4-treated mice for biosafety evaluation (n = 3); scale bar: 20 μm. This analysis assesses the histopathological effects and biocompatibility of the nanoparticle formulations.

contrast enhancement (Figure 5b,c). In vivo, T2-weighted MRI was performed on 4T1 tumor-bearing Balb/c mice to evaluate the tumor-targeting efficiency of the nanoparticles. Mice treated with peptide-SLN-OA-Fe_3O_4 demonstrated a time-dependent (30, 60, and 180 min) accumulation of the nanoparticles in tumor tissues, leading to enhanced MRI contrast. In comparison, mice treated with nontargeted SLN-OA-Fe_3O_4 showed a more diffuse distribution, with greater accumulation in off-target organs such as the liver. After 180 min postinjection, peptide-SLN-OA-Fe_3O_4 exhibited significantly higher accumulation in tumor tissues, providing superior contrast compared to nontargeted nanoparticles (Figure 5d). These findings confirm that the peptide-functionalized nanoparticles offer enhanced tumor targeting, making them suitable for diagnostic imaging of TNBC.

3.5. In Vivo SPECT Imaging. SPECT imaging was conducted to obtain more detailed insights into the distribution patterns of ^{99m}Tc-labeled nanoparticles, as shown in Movies S1 (mice treated with free ^{99m}Tc), S2 (mice treated with ^{99m}Tc-SLN-OA-Fe_3O_4), and S3 (mice treated with ^{99m}Tc-peptide-SLN-OA-Fe_3O_4). Figure 6a illustrates the procedural details for both radiolabeling and SPECT imaging conducted in living organisms. At 1 h following the injection, the peptide-SLN-OA-Fe_3O_4 formulation exhibited a notably greater accumulation within tumor tissues in comparison with both the free ^{99m}Tc and SLN-OA-Fe_3O_4 nanoparticles, which lacked peptide conjugation. The free ^{99m}Tc was quickly eliminated from the blood circulation and was found to accumulate mainly in the bladder. Conversely, the SLN-OA-Fe_3O_4 nanoparticles were primarily found in the liver, with only minimal accumulation observed in the tumor, which can be attributed to a passive targeting mechanism. The formulation that included the peptide demonstrated an increased buildup specifically in tumor areas, which verified the high efficiency of the C-peptide in targeting integrin $\alpha v\beta_3$ receptors when introduced to a living system, as evidenced in Figure 6b.

https://doi.org/10.1021/acsomega.4c10153
ACS Omega 2025, 10, 17310−17326

3.6. Biodistribution and Targeting Efficacy. The biodistribution and targeting specificity of the nanoparticles were assessed using Prussian blue staining and radioactivity analysis. The results showed a significantly higher accumulation of iron particles in the tumor tissues of mice treated with peptide-SLN-OA-Fe_3O_4 compared to those treated with SLN-OA-Fe_3O_4, with the difference becoming more pronounced over time (Figure 7a). At 30 min postinjection, the mean tumor iron accumulation was 30% ID/tissue for peptide-functionalized nanoparticles, compared to only 2% ID/tissue for the nontargeted nanoparticles. This difference grew at 60 min (39 vs 3% ID/tissue) and at 180 min (55 vs 5% ID/tissue), indicating an 11-fold improvement in tumor targeting efficiency for the peptide-coated formulation by the final time point. In contrast, liver accumulation followed an opposite trend. At 30 min, the mean iron particle levels in the liver were 27% ID/tissue for peptide-SLN-OA-Fe_3O_4 and 45% ID/tissue for SLN-OA-Fe_3O_4. These levels decreased to 23 vs 33% ID/tissue at 60 min and further dropped to 16.3 vs 31.6% ID/tissue at 180 min. This progressive reduction in liver sequestration for peptide-coated nanoparticles contrasts sharply with the sustained hepatic retention observed for nontargeted nanoparticles. Quantitative analysis confirmed that the iron particle concentration in the tumors of peptide-SLN-OA-Fe_3O_4-treated mice was significantly higher, demonstrating effective tumor targeting and reduced liver accumulation, thus minimizing hepatic sequestration (Figure 7b). However, the biodistribution analysis also revealed substantial accumulation of SLN-OA-Fe_3O_4 in the kidneys, as shown in Figure 8a,b. At 180 min postinjection, the mean iron particle accumulation in the kidneys was 14.3% ID/tissue for peptide-SLN-OA-Fe_3O_4, compared to 28.6% ID/tissue for SLN-OA-Fe_3O_4. While peptide-SLN-OA-Fe_3O_4 shows improved tumor targeting and fewer off-target effects, significant retention of SLN-OA-Fe_3O_4 in the kidneys raises important considerations regarding potential filtration and clearance mechanisms. These findings underscore the targeted delivery capabilities of peptide-SLN-OA-Fe_3O_4 and highlight the need for further evaluation of kidney accumulation in future therapeutic studies. Additionally, quantitative biodistribution analysis using a dose calibrator validated the SPECT imaging results, confirming the superior tumor targeting of ^{99m}Tc-pPeptide-SLN-OA-Fe_3O_4 in the tissues of treated mice (Figure 6c). Prussian blue staining and SPECT imaging corroborated the MRI findings, revealing significant iron particle accumulation in tumors with reduced hepatic sequestration from peptide-SLN-OA-Fe_3O_4 nanoparticles. The greater tumor uptake of ^{99m}Tc-peptide-SLN-OA-Fe_3O_4 compared to ^{99m}Tc-SLN-OA-Fe_3O_4 further highlights the effectiveness and specificity of this targeted delivery system. Based on calculations using eqs 2 and 3 in Section 2, the blood clearance rate of the ^{99m}Tc-labeled solid lipid nanoparticles (SLNs) was determined to be 1 mCi/h. As observed in the biodistribution analysis, the radioactivity levels in blood samples taken from the mouse groups treated with ^{99m}Tc-labeled SLNs were nearly undetectable after 1 h, indicating that the nanoparticles had cleared from circulation.

The developed nanoparticles, which integrate SPIONs for MRI contrast and ^{99m}Tc for SPECT imaging, provide a comprehensive platform for monitoring the biodistribution and confirming targeted delivery. This approach enhances the early diagnosis, precise treatment, and real-time monitoring of therapeutic efficacy in breast cancer. Optimizing nanoparticle excretion pathways is crucial for minimizing liver accumulation and maximizing targeting efficacy, ensuring safe elimination after treatment.[48]

3.7. Biosafety. 4T1MCT-bearing mice treated with SLN-Fe_3O_4 and peptide-SLN-OA-Fe_3O_4 nanoparticles underwent biosafety evaluation. To this end, H&E staining was conducted on tissue samples, including the lung, kidney, spleen, liver, and heart tissues (Figure 9). The alveolar structure in the lung tissue of both the SLN-OA-Fe_3O_4 and peptide-SLN-OA-Fe_3O_4 treated groups appears largely similar to that in the normal lung tissue, with open air spaces and no obvious signs of alveolar damage, inflammation, or thickening.[49−52] In the kidney, the renal corpuscles (glomeruli) and tubules show typical morphology in all groups, with no apparent signs of glomerular sclerosis, tubular damage, or interstitial inflammation.[22,53] The spleen architecture, including the white pulp (lymphoid follicles) and red pulp (sinusoids), appears comparable between the treated and control groups, with no observable changes in cellularity or signs of congestion.[54] In the liver, the hepatic lobules, central veins, and sinusoids appear normal in the treated groups, with no evidence of hepatocyte necrosis, steatosis (fatty changes), or inflammatory cell infiltration.[22,53] Examination of the heart reveals that the cardiomyocytes display normal morphology with intact striations and no apparent signs of cellular damage, inflammation, or fibrosis in the treated groups.[55] These observations suggest that the SLN nanoparticle formulations, both with and without peptide modification, exhibit a favorable biosafety profile for in vivo diagnostic applications, as evidenced by the absence of significant histopathological abnormalities in major organs of treated mice compared to normal controls.[56,57]

4. CONCLUSIONS

This study successfully demonstrates the innovative use of integrin-targeted SLNs conjugated with a C-terminal peptide derived from endostatin as a powerful tool for enhancing dual-modality imaging of TNBC. The SLNs exhibited remarkable stability, biocompatibility, and optimal magnetic properties, enabling efficient accumulation in tumor sites through selective targeting of integrin $\alpha v\beta_3$. In vitro and in vivo evaluations confirmed that peptide-conjugated SLNs significantly improve imaging contrast and tumor localization compared to their nontargeted counterparts, marking a substantial advancement in the diagnostic capabilities for TNBC.

The implications of these findings are profound, as they suggest that such targeted imaging agents could not only facilitate earlier detection of TNBC but also inform treatment strategies by providing real-time monitoring of therapeutic efficacy. As we move forward, further optimization of these nanoparticles is essential to enhance their excretion pathways, ensuring minimal off-target effects and improved patient safety. This work paves the way for future translational applications of peptide-functionalized nanomedicines in cancer diagnosis and treatment, highlighting a promising frontier in personalized oncology. The integration of imaging techniques with targeted therapy underscores a significant step toward overcoming the challenges posed by aggressive cancer subtypes like TNBC, ultimately striving for better patient outcomes and survival rates.

https://doi.org/10.1021/acsomega.4c10153
ACS Omega 2025, 10, 17310−17326

■ ASSOCIATED CONTENT

Data Availability Statement

Data supporting this study's findings are available in the Supporting Information.

Supporting Information

The Supporting Information is available free of charge at https://pubs.acs.org/doi/10.1021/acsomega.4c10153.

Schematic of the protocol for the synthesis of Fe_3O_4 nanoparticles and oleic acid coating; schematic of SLN-OA-Fe_3O_4 synthesis; schematic representation of C-peptide conjugation with SLN synthesis; LC−MS spectrum of C-peptide; HPLC spectrum of C-peptide; molecular modeling of C-peptide; magnetic properties of OA−Fe_3O_4 nanoparticles using an external magnet; size and polydispersity index determination of synthetic nanoparticles via DLS; ζ-potential of synthetic nanoparticles measured by DLS; storage stability analysis of nanoparticles; morphological characterization of nanoparticles; and cell viability test (PDF)

SPECT image showing the distribution pattern of ^{99m}Tc-labeled nanoparticles (MP4)

SPECT image showing the distribution pattern of ^{99m}Tc-labeled nanoparticles (MP4)

SPECT image showing the distribution pattern of ^{99m}Tc-labeled nanoparticles (MP4)

■ AUTHOR INFORMATION

Corresponding Authors

Hossein Ghafouri − *Department of Biology, Faculty of Sciences, University of Guilan, 4199613776 Rasht, Iran;* orcid.org/0000-0003-2245-0697; Email: h.ghafoori@guilan.ac.ir

S. Mohsen Asghari − *Institute of Biochemistry and Biophysics, University of Tehran, 1411713135 Tehran, Iran;* orcid.org/0000-0002-0782-6687; Email: sm.asghari@ut.ac.ir

Authors

Tahereh Rahdari − *Department of Biology, Faculty of Sciences, University of Guilan, 4199613776 Rasht, Iran*

Sorour Ramezanpour − *Department of Chemistry, K. N. Toosi University of Technology, 158754416 Tehran, Iran;* orcid.org/0000-0002-3901-0391

Mehdi Shafiee Ardestani − *Department of Radiopharmacy, Faculty of Pharmacy, Tehran University of Medical Sciences, 1461884513 Tehran, Iran; Research Center for Nuclear Medicine, Shariati Hospital, 1411713135 Tehran, Iran*

Complete contact information is available at: https://pubs.acs.org/10.1021/acsomega.4c10153

Notes

Ethics Approval: All animal experiments were conducted following ethical guidelines and with approval from the Ethics Committee in Biomedical Research at the University of Guilan (Approval code: IR.GUILAN.REC.1401.010).

The authors declare no competing financial interest.

■ ACKNOWLEDGMENTS

We express our gratitude to the individuals and institutions supporting this research, particularly the University of Tehran and the University of Guilan. Special thanks are due to the Preclinical Lab at Tehran University of Medical Sciences, the National Brain Mapping Laboratory, and MRI Center Institute of Tehran for their in vivo imaging services, as well as the Animal Core Facility at the Institute of Biochemistry and Biophysics, University of Tehran, for their technical expertise.

■ REFERENCES

(1) Liu, C.; Zhao, Z.; Gao, R.; Zhang, X.; Sun, Y.; Wu, J.; Liu, J.; Chen, C. Matrix metalloproteinase-2-responsive surface-changeable liposomes decorated by multifunctional peptides to overcome the drug resistance of triple-negative breast cancer through enhanced targeting and penetrability. *ACS Biomater. Sci. Eng.* **2022**, *8* (7), 2979−2994.

(2) Wu, X.; Han, Z.; Schur, R. M.; Lu, Z.-R. Targeted mesoporous silica nanoparticles delivering arsenic trioxide with environment sensitive drug release for effective treatment of triple negative breast cancer. *ACS Biomater. Sci. Eng.* **2016**, *2* (4), 501−507.

(3) Zheng, X.-C.; Ren, W.; Zhang, S.; Zhong, T.; Duan, X.-C.; Yin, Y.-F.; Xu, M.-Q.; Hao, Y.-L.; Li, Z.-T.; Li, H. The theranostic efficiency of tumor-specific, pH-responsive, peptide-modified, liposome-containing paclitaxel and superparamagnetic iron oxide nanoparticles. *Int. J. Nanomed.* **2018**, *13*, 1495−1504.

(4) Yu, S.; Huang, G.; Yuan, R.; Chen, T. A uPAR targeted nanoplatform with an NIR laser-responsive drug release property for tri-modal imaging and synergistic photothermal-chemotherapy of triple-negative breast cancer. *Biomater. Sci.* **2020**, *8* (2), 720−738.

(5) Mohajeri, M.; Salehi, P.; Heidari, B.; Rafati, H.; Asghari, S. M.; Behboudi, H.; Iranpour, P. PEGylated Pemetrexed and PolyNIPAM Decorated Gold Nanoparticles: A Biocompatible and Highly Stable CT Contrast Agent for Cancer Imaging. *ACS Appl. Bio Mater.* **2024**, *7* (9), 5977−5991.

(6) Xiao, Y.-T.; Zhou, C.; Ye, J.-C.; Yang, X.-C.; Li, Z.-J.; Zheng, X.-B.; Mei, Y.; Li, X.-L.; Zhang, W.-G.; Fan, W. Integrin α6-targeted positron emission tomography imaging of colorectal cancer. *ACS Omega* **2019**, *4* (13), 15560−15566.

(7) Steyerova, P.; Burgetova, A. Current imaging techniques and impact on diagnosis and survival—a narrative review. *Ann. Breast Surg.* **2022**, *6*, No. 25, DOI: 10.21037/abs-21-22.

(8) Frascione, D.; Diwoky, C.; Almer, G.; Opriessnig, P.; Vonach, C.; Gradauer, K.; Leitinger, G.; Mangge, H.; Stollberger, R.; Prassl, R. Ultrasmall superparamagnetic iron oxide (USPIO)-based liposomes as magnetic resonance imaging probes. *Int. J. Nanomed.* **2012**, *7*, 2349−2359.

(9) Yang, L.; Tang, J.; Yin, H.; Yang, J.; Xu, B.; Liu, Y.; Hu, Z.; Yu, B.; Xia, F.; Zou, G. Self-assembled nanoparticles for tumor-triggered targeting dual-mode NIRF/MR imaging and photodynamic therapy applications. *ACS Biomater. Sci. Eng.* **2022**, *8* (2), 880−892.

(10) Alnasraui, A. H. F.; Joe, I. H.; Al-Musawi, S. Investigation of Folate-Functionalized Magnetic-Gold Nanoparticles Based Targeted Drug Delivery for Liver: In Vitro, In Vivo and Docking Studies. *ACS Biomater. Sci. Eng.* **2024**, *10* (10), 6299−6313.

(11) Wei, X.; Zhao, H.; Huang, G.; Liu, J.; He, W.; Huang, Q. ESMION-based dual-modality PET/MRI probes for acidic tumor microenvironment imaging. *ACS Omega* **2022**, *7* (4), 3442−3451.

(12) Eroglu, H.; Yenilmez, A. An Investigation of the Usability of Solid Lipid Nanoparticles Radiolabelled with Tc-99m as Imaging Agents in Liver-Spleen Scintigraphy. *J. Biomed. Nanotechnol.* **2016**, *12* (7), 1501−1509.

(13) Andreozzi, E.; Seo, J. W.; Ferrara, K.; Louie, A. Novel method to label solid lipid nanoparticles with 64cu for positron emission tomography imaging. *Bioconjugate Chem.* **2011**, *22* (4), 808−818.

(14) Liu, H.; Zhang, M.; Jin, H.; Tao, K.; Tang, C.; Fan, Y.; Liu, S.; Liu, Y.; Hou, Y.; Zhang, H. Fe(III)-doped Polyaminopyrrole nanoparticle for imaging-guided Photothermal therapy of bladder cancer. *ACS Biomater. Sci. Eng.* **2022**, *8* (2), 502−511.

(15) Zargari, N. R.; Ebrahimi, F.; Akhlaghi, M.; Beiki, D.; Abdi, K.; Abbasi, M. A.; Ramezanpour, S.; Asghari, S. M. Novel Gd-DTPA-peptide for targeted breast tumor magnetic resonance imaging. *Biomed. Pharmacother.* **2024**, *178*, No. 117189.

(16) Ayan, A. K.; Yenilmez, A.; Eroglu, H. Evaluation of radiolabeled curcumin-loaded solid lipid nanoparticles usage as an imaging agent in liver-spleen scintigraphy. *Mater. Sci. Eng., C* **2017**, *75*, 663−670.
(17) Zanjanchi, P.; Asghari, S. M.; Mohabatkar, H.; Shourian, M.; Shafiee Ardestani, M. Conjugation of VEGFR1/R2-targeting peptide with gold nanoparticles to enhance antiangiogenic and antitumoral activity. *J. Nanobiotechnol.* **2022**, *20*, 7.
(18) Chamani, R.; Asghari, S. M.; Alizadeh, A. M.; Eskandari, S.; Mansouri, K.; Khodarahmi, R.; Taghdir, M.; Heidari, Z.; Gorji, A.; Aliakbar, A.; et al. Engineering of a disulfide loop instead of a Zn binding loop restores the anti-proliferative, anti-angiogenic and anti-tumor activities of the N-terminal fragment of endostatin: Mechanistic and therapeutic insights. *Vasc. Pharmacol.* **2015**, *72*, 73−82.
(19) Chamani, R.; Asghari, S. M.; Alizadeh, A. M.; Mansouri, K.; Doroudi, T.; Kolivand, P. H.; Ghafouri, H.; Ehtesham, S.; Rabouti, H.; Mehrnejad, F. The antiangiogenic and antitumor activities of the N-terminal fragment of endostatin augmented by Ile/Arg substitution: the overall structure implicated the biological activity. *Biochim. Biophys. Acta, Proteins Proteomics* **2016**, *1864* (12), 1765−1774.
(20) Ehtesham, S.; Sariri, R.; Eidi, A.; Hosseinkhani, S. Functional Studies on a Novel Engineered Peptide Derived from C-Terminal of Human Endostatin. *Biomacromol. J.* **2018**, *4* (1), 58−64.
(21) Rahdari, T.; Mahdavimehr, M.; Ghafouri, H.; Ramezanpour, S.; Ehtesham, S.; Asghari, S. M. Advancing triple-negative breast cancer treatment through peptide decorated solid lipid nanoparticles for paclitaxel delivery. *Sci. Rep.* **2025**, *15* (1), No. 6043.
(22) Mahdavimehr, M.; Rahdari, T.; Nikfarjam, N.; Ehtesham, S.; Ardestani, M. S.; Asghari, S. M. Development and application of dual-modality tumor-targeting SPIONs for precision breast cancer imaging. *Biomater. Adv.* **2025**, *172*, No. 214236.
(23) Lee, W. W.; Group, K.-S. Clinical applications of technetium-99m quantitative single-photon emission computed tomography/computed tomography. *Nucl. Med. Mol. Imaging* **2019**, *53* (3), 172−181.
(24) Bonvin, D.; Hofmann, H.; Mionic Ebersold, M. Optimisation of aqueous synthesis of iron oxide nanoparticles for biomedical applications. *J. Nanopart. Res.* **2016**, *18*, No. 376.
(25) Kuo, Y.-C.; Lee, C.-H.; Rajesh, R. Iron oxide-entrapped solid lipid nanoparticles and poly (lactide-co-glycolide) nanoparticles with surfactant stabilization for antistatic application. *J. Mater. Res. Technol.* **2019**, *8* (1), 887−895.
(26) Girotra, P.; Singh, S. K. Multivariate optimization of rizatriptan benzoate-loaded solid lipid nanoparticles for brain targeting and migraine management. *AAPS PharmSciTech* **2017**, *18* (2), 517−528.
(27) Miner, M. W. G.; Liljenbäck, H.; Virta, J.; Helin, S.; Eskola, O.; Elo, P.; Teuho, J.; Seppälä, K.; Oikonen, V.; Yang, G.; et al. Comparison of: (2S,4R)-4-[18F]Fluoroglutamine, [11C]Methionine, and 2-Deoxy-2-[18F]Fluoro-D-Glucose and two small-animal PET/CT systems imaging rat gliomas. *Front. Oncol.* **2021**, *11*, No. 730358.
(28) Baek, J.-S.; Cho, C.-W. Controlled release and reversal of multidrug resistance by co-encapsulation of paclitaxel and verapamil in solid lipid nanoparticles. *Int. J. Pharm.* **2015**, *478* (2), 617−624.
(29) Mulik, R. S.; Mönkkönen, J.; Juvonen, R. O.; Mahadik, K. R.; Paradkar, A. R. Transferrin mediated solid lipid nanoparticles containing curcumin: enhanced in vitro anticancer activity by induction of apoptosis. *Int. J. Pharm.* **2010**, *398* (1−2), 190−203.
(30) Lasa-Saracíbar, B.; El Moukhtari, S. H.; Tsotakos, T.; Xanthopoulos, S.; Loudos, G.; Bouziotis, P.; Blanco-Prieto, M. J. In vivo biodistribution of edelfosine-loaded lipid nanoparticles radiolabeled with Technetium-99 m: Comparison of administration routes in mice. *Eur. J. Pharm. Biopharm.* **2022**, *175*, 1−6.
(31) Assareh, E.; Mehrnejad, F.; Mansouri, K.; Esmaeili Rastaghi, A. R.; Naderi-Manesh, H.; Asghari, S. M. A cyclic peptide reproducing the α1 helix of VEGF-B binds to VEGFR-1 and VEGFR-2 and inhibits angiogenesis and tumor growth. *Biochem. J.* **2019**, *476* (4), 645−663.
(32) Farzaneh Behelgardi, M.; Zahri, S.; Mashayekhi, F.; Mansouri, K.; Asghari, S. M. A peptide mimicking the binding sites of VEGF-A and VEGF-B inhibits VEGFR-1/-2 driven angiogenesis, tumor growth and metastasis. *Sci. Rep.* **2018**, *8* (1), No. 17924.
(33) Li, D.; Dong, C.; Ma, X.; Zhao, X. Integrin $\alpha v\beta 6$-targeted MR molecular imaging of breast cancer in a xenograft mouse model. *Cancer Imaging* **2021**, *21* (1), No. 44.
(34) Semete, B.; Booysen, L.; Kalombo, L.; Venter, J. D.; Katata, L.; Ramalapa, B.; Verschoor, J. A.; Swai, H. In vivo uptake and acute immune response to orally administered chitosan and PEG coated PLGA nanoparticles. *Toxicol. Appl. Pharmacol.* **2010**, *249* (2), 158−165.
(35) de Mendoza, A. E.-H.; Rayo, M.; Mollinedo, F.; Blanco-Prieto, M. J. Lipid nanoparticles for alkyl lysophospholipid edelfosine encapsulation: development and in vitro characterization. *Eur. J. Pharm. Biopharm.* **2008**, *68* (2), 207−213.
(36) Schwarz, C. Solid lipid nanoparticles (SLN) for controlled drug delivery II. Drug incorporation and physicochemical characterization. *J. Microencapsulation* **1999**, *16* (2), 205−213.
(37) Xiao, K.; Li, Y.; Luo, J.; Lee, J. S.; Xiao, W.; Gonik, A. M.; Agarwal, R. G.; Lam, K. S. The effect of surface charge on in vivo biodistribution of PEG-oligocholic acid based micellar nanoparticles. *Biomaterials* **2011**, *32* (13), 3435−3446.
(38) Patel, M. N.; Lakkadwala, S.; Majrad, M. S.; Injeti, E. R.; Gollmer, S. M.; Shah, Z. A.; Boddu, S. H. S.; Nesamony, J. Characterization and evaluation of 5-fluorouracil-loaded solid lipid nanoparticles prepared via a temperature-modulated solidification technique. *Aaps PharmSciTech* **2014**, *15*, 1498−1508.
(39) Mohseni, R.; ArabSadeghabadi, Z.; Ziamajidi, N.; Abbasalipourkabir, R.; RezaeiFarimani, A. Oral administration of resveratrol-loaded solid lipid nanoparticle improves insulin resistance through targeting expression of SNARE proteins in adipose and muscle tissue in rats with type 2 diabetes. *Nanoscale Res. Lett.* **2019**, *14*, No. 227.
(40) Thapa, B.; Diaz-Diestra, D.; Beltran-Huarac, J.; Weiner, B. R.; Morell, G. Enhanced MRI T 2 relaxivity in contrast-probed anchor-free PEGylated iron oxide nanoparticles. *Nanoscale Res. Lett.* **2017**, *12*, No. 312.
(41) Taheri-Ledari, R.; Zhang, W.; Radmanesh, M.; Mirmohammadi, S. S.; Maleki, A.; Cathcart, N.; Kitaev, V. Multi-stimuli nanocomposite therapeutic: docetaxel targeted delivery and synergies in treatment of human breast cancer tumor. *Small* **2020**, *16* (41), No. 2002733.
(42) Patil, R. M.; Shete, P.; Thorat, N.; Otari, S.; Barick, K.; Prasad, A.; Ningthoujam, R.; Tiwale, B.; Pawar, S. Non-aqueous to aqueous phase transfer of oleic acid coated iron oxide nanoparticles for hyperthermia application. *RSC Adv.* **2014**, *4* (9), 4515−4522.
(43) Nguyen, M. D.; Deng, L.; Lee, J. M.; Resendez, K. M.; Fuller, M.; Hoijang, S.; Robles-Hernandez, F.; Chu, C. W.; Litvinov, D.; Hadjiev, V. G.; et al. Magnetic Tunability via Control of Crystallinity and Size in Polycrystalline Iron Oxide Nanoparticles. *Small* **2024**, *20*, No. 2402940.
(44) Cai, J.; Miao, Y. Q.; Yu, B. Z.; Ma, P.; Li, L.; Fan, H. M. Large-scale, facile transfer of oleic acid-stabilized iron oxide nanoparticles to the aqueous phase for biological applications. *Langmuir* **2017**, *33* (7), 1662−1669.
(45) Gao, S.; Lin, H.; Zhang, H.; Yao, H.; Chen, Y.; Shi, J. Nanocatalytic tumor therapy by biomimetic dual inorganic nanozyme-catalyzed cascade reaction. *Adv. Sci.* **2019**, *6* (3), No. 1801733.
(46) Zhu, X.; Deng, X.; Lu, C.; Chen, Y.; Jie, L.; Zhang, Q.; Li, W.; Wang, Z.; Du, Y.; Yu, R. SPIO-loaded nanostructured lipid carriers as liver-targeted molecular T2-weighted MRI contrast agent. *Quant. Imaging Med. Surg.* **2018**, *8* (8), 770.
(47) Rostaminasab, S.; Esmaeili, A.; Moosavi-Movahedi, F.; Memarkashani, S.; Rudmianeh, H. R.; Shourian, M.; Ardestani, M. S.; Moosavi-Movahedi, A. A.; Asghari, S. M. Enhanced antitumor activity of lapatinib against triple-negative breast cancer via loading in human serum albumin. *Int. J. Biol. Macromol.* **2024**, *282*, No. 136760.
(48) Seo, H. J.; Nam, S. H.; Im, H.-J.; Park, J.-y.; Lee, J. Y.; Yoo, B.; Lee, Y.-S.; Jeong, J. M.; Hyeon, T.; Who Kim, J.; et al. Rapid hepatobiliary excretion of micelle-encapsulated/radiolabeled upcon-

https://doi.org/10.1021/acsomega.4c10153
ACS Omega 2025, 10, 17310−17326

verting nanoparticles as an integrated form. *Sci. Rep.* **2015**, *5* (1), No. 15685.
(49) da Rocha, M. C. O.; da Silva, P. B.; Radicchi, M. A.; Andrade, B. Y. G.; de Oliveira, J. V.; Venus, T.; Merker, C.; Estrela-Lopis, I.; Longo, J. P. F.; Báo, S. N. Docetaxel-loaded solid lipid nanoparticles prevent tumor growth and lung metastasis of 4T1 murine mammary carcinoma cells. *J. Nanobiotechnol.* **2020**, *18*, No. 43.
(50) Ma, T.; Tang, Y.; Wang, T.; Yang, Y.; Zhang, Y.; Wang, R.; Zhang, Y.; Li, Y.; Wu, M.; Tang, M.; et al. Chronic pulmonary bacterial infection facilitates breast cancer lung metastasis by recruiting tumor-promoting MHCIIhi neutrophils. *Signal Transduction Targeted Ther.* **2023**, *8* (1), 296.
(51) Ye, T.; Xiong, Y.; Yan, Y.; Xia, Y.; Song, X.; Liu, L.; Li, D.; Wang, N.; Zhang, L.; Zhu, Y.; et al. The anthelmintic drug niclosamide induces apoptosis, impairs metastasis and reduces immunosuppressive cells in breast cancer model. *PLoS One* **2014**, *9* (1), No. e85887.
(52) Shi, Z.; Luo, M.; Huang, Q.; Ding, C.; Wang, W.; Wu, Y.; Luo, J.; Lin, C.; Chen, T.; Zeng, X.; et al. NIR-dye bridged human serum albumin reassemblies for effective photothermal therapy of tumor. *Nat. Commun.* **2023**, *14* (1), No. 6567.
(53) Khan, F.; Khan, T. J.; Kalamegam, G.; Pushparaj, P. N.; Chaudhary, A.; Abuzenadah, A.; Kumosani, T.; Barbour, E.; Al-Qahtani, M. Anti-cancer effects of Ajwa dates (*Phoenix dactylifera* L.) in diethylnitrosamine induced hepatocellular carcinoma in Wistar rats. *BMC Complementary Altern. Med.* **2017**, *17*, No. 418.
(54) Wang, H.; Li, S.; Cui, Z.; Qin, T.; Shi, H.; Ma, J.; Li, L.; Yu, G.; Jiang, T.; Li, C. Analysis of spleen histopathology, splenocyte composition and haematological parameters in four strains of mice infected with *Plasmodium berghei* K173. *Malar. J.* **2021**, *20*, No. 249.
(55) Castrogiovanni, P.; Trovato, F. M.; Szychlinska, M. A.; Loreto, C.; Giunta, S.; Scuderi, S.; Passanisi, R.; Fidone, F.; Fagone, P.; Imbesi, R.; et al. Effects of synthetic anti-inflammatory sterol in CB3V-induced myocarditis: a morphological study on heart muscle tissue. *J. Funct. Morphol. Kinesiol.* **2016**, *1* (1), 69−89.
(56) Liu, C.; Zou, Q.; Tang, H.; Liu, J.; Zhang, S.; Fan, C.; Zhang, J.; Liu, R.; Liu, Y.; Liu, R.; et al. Melanin nanoparticles alleviate sepsis-induced myocardial injury by suppressing ferroptosis and inflammation. *Bioact. Mater.* **2023**, *24*, 313−321.
(57) Pi, F.; Deng, X.; Xue, Q.; Zheng, L.; Liu, H.; Yang, F.; Chen, T. Alleviating the hypoxic tumor microenvironment with MnO2-coated CeO2 nanoplatform for magnetic resonance imaging guided radiotherapy. *J. Nanobiotechnol.* **2023**, *21* (1), 90.

https://doi.org/10.1021/acsomega.4c10153
ACS Omega 2025, 10, 17310−17326